Tensile Material Properties of Human Costal Cartilage Perichondrium

Julia Anne Damron

Thesis submitted to the faculty of the Virginia Polytechnic Institute and State University in partial fulfillment of the requirements for the degree of

Master of Science

In

Biomedical Engineering

Devon L. Albert, Ph.D., Chair

Andrew R. Kemper, Ph.D.

Warren N. Hardy, Ph.D.

Amanda M. Agnew, Ph.D.

May 3, 2024

Blacksburg, VA

Keywords: perichondrium, cartilage, thorax, thoracic injury, biomechanics, stress, strain, tension

Tensile Material Properties of Human Costal Cartilage Perichondrium

Julia Anne Damron

ACADEMIC ABSTRACT

Rib and costal cartilage fractures are the most common injuries resulting from blunt thoracic loading scenarios, including motor vehicle collisions. The costal cartilage is a cylindrical hyaline cartilage composed of two layers: a core interstitial matrix enveloped by the perichondrium. The perichondrium itself has an inner chondrogenic layer and an outer fibrous layer. The objective of this study was to evaluate the tensile material properties of human costal cartilage perichondrium at two loading rates for a range of subject demographics. Fifty-six (n=56) samples containing the fibrous layer and chondrogenic layer (i.e., two-layered samples) were fabricated from thirty-three (n=33) donors aged from 11 to 69 years of age (19 M, 14 F). Thirteen (n=13) samples without the fibrous layer (i.e., one-layered samples) were fabricated from eight (n=8) donors aged from 11 to 54 years of age (5 M, 3 F). The perichondrium was isolated from the interstitial matrix for all samples and the fibrous layer was removed for one-layered samples to assess the effect of the absence of the fibrous layer. The tissue was then stamped into a dog bone-shaped coupon and sanded down to a uniform thickness of ~1.3 mm for two-layered samples and ~1 mm for one-layered samples. The gage length of the completed coupons was marked with a black ink dot pattern to facilitate strain calculations via video tracking. The coupons were loaded axially in tension to failure at either a slow (0.005 s^{-1}) or fast (0.5 s^{-1}) target loading rate using a material testing system. The elastic modulus, ultimate stress, ultimate strain, failure stress, failure strain, and strain energy density (SED) were then calculated for each test. Material property data were compared by sample type and loading rate. Since there was no significant influence of sex on any material properties, the data were grouped together for the analysis. Modulus, ultimate stress, failure stress, and SED were found to significantly decrease with donor age at both loading rates and ultimate and failure strain also significantly decreased with donor age at the 0.5 s^{-1} target loading rate. Failure stress in the two-layered samples was found to be greater than that of the one-layered samples at both loading rates. One-layered samples had a greater failure strain than two-layered samples at both loading rates. Perichondrium data were compared to interstitial matrix data from a previous study to further investigate the role of cartilage layer on material properties. The modulus, ultimate stress, and failure stress of costal cartilage decreased moving radially inward (greatest in two-layered perichondrium samples, least in interstitial matrix samples). The opposite was true for ultimate and failure strain, with the greatest failure strain values occurring in the interstitial matrix and the least in the two-layered perichondrium samples. The sample size of one-layered samples was too small to draw any substantial conclusions regarding age trends. This was the first study to analyze the material property trends in costal cartilage perichondrium. The results of this study can be incorporated into virtual human body models to improve the accuracy of thoracic injury prediction in the context of motor vehicle safety.

Tensile Material Properties of Human Costal Cartilage Perichondrium

Julia Anne Damron

GENERAL AUDIENCE ABSTRACT

Motor vehicle collisions are the second leading cause of death due to unintentional injury in the United States, with rib and costal cartilage fractures being the most commonly observed injuries. The cylindrical costal cartilage connects the front of the ribs to the sternum and is composed of two layers: a core interstitial matrix enveloped by the perichondrium. The perichondrium itself has an inner chondrogenic layer and an outer fibrous layer. Virtual human body models incorporate material property data to improve their ability to predict injury risk and are frequently used among vehicle manufacturers to evaluate safety during vehicle development. Currently, models have to make simplifications and assumptions regarding the perichondrium properties, since there are no material property studies on the isolated perichondrium to date. Therefore, the purpose of this study was to quantify the tensile material properties of human costal cartilage perichondrium at two loading rates for a range of subject demographics. Dog-bone shaped coupons with either both perichondrium layers (i.e., two-layered samples) or just the chondrogenic layer (i.e., one-layered samples) were loaded to failure under tension at either a slow (0.005 s^{-1}) or fast (0.5 s^{-1}) target loading rate using a material testing system. Data were obtained for fifty-six (n=56) two-layered samples from thirty-three (n=33) donors aged from 11 to 69 years old. Data were collected for thirteen (n=13) one-layered samples from eight (n=8) donors aged from 11 to 54 years old. The elastic modulus, ultimate stress, ultimate strain, failure stress, failure strain, and strain energy density (SED) were quantified for each test. Material properties of two-layered samples decreased with increasing donor age. No trends were found with regard to donor sex. Only ultimate and failure stress of two-layered samples were significantly affected by loading rate. Perichondrium material property data were compared to interstitial matrix data from a previous study to investigate the effect of cartilage layer on costal cartilage material properties. Elastic modulus, ultimate stress, and failure stress decreased when moving inward in cartilage layers, while ultimate and failure strain increased. Overall, this is the first study to evaluate the material properties of the perichondrium and the change in material properties with cartilage layer. These data can be used to improve the accuracy of human tolerance to thoracic injury in human body models.

ACKNOWLEDGEMENTS

I would first like to thank my thesis advisor, Dr. Devon Albert, for all of the guidance she has given me in the last two years. I owe much of my success to her kindness and mentorship in navigating my Master's degree. I would also like to give special thanks to Dr. Andrew Kemper, who was my advisor during my first year of graduate school. Thanks to my other committee members, Dr. Amanda Agnew and Dr. Warren Hardy, for their time and contributions.

I would also like to thank my family, friends, and labmates for their support during this research.

Finally, I would like to thank the anatomical donors, without whose generous gifts this research would not have been possible.

TABLE OF CONTENTS

LIST OF FIGURES

LIST OF TABLES

Introduction

Motor vehicle collisions (MVCs) are the second leading cause of death due to unintentional injury [1] and the third leading cause of nonfatal emergency room visits in the United States [2]. Thorax injury is a leading cause of fatality in MVCs [3], and rib and costal cartilage fractures are the most common injuries resulting from blunt thoracic trauma [4], [5], [6]. Studies have shown that the thorax is not only the most fatally injured but also the most commonly injured body region for rear seat occupants in MVCs, regardless of whether the occupant was belted at the time of collision [7]. Rear seat occupants in particular experience a greater level of concentrated loading to the thorax from the seat belt in frontal impacts due to the lack of rear seat airbags when compared to front seat occupants in the same collision [8]. Rib fractures are also the most common occurrence of AIS3+ injury to the thorax on the Abbreviated Injury Scale (AIS) [6], [9]. Fractures in the costal cartilage, which connects the ribs to the sternum, are categorized as rib fractures according to the current AIS injury scale and contribute equally to the thoracic injury severity rating [10].

The skeletal structure of the human thorax features the ribs, sternal assembly, thoracic vertebrae of the spine, and costal cartilage. There are 12 thoracic vertebrae, each connected posteriorly to a pair of ribs. The ribs are connected anteriorly to costal cartilage at costochondral junctions, and the costal cartilage are connected to the sternal assembly at costosternal junctions. The sternal assembly contains the manubrium at the top, the sternum or sternal body in the middle, and the xiphoid process at the bottom. The clavicle and ribs 1-2 attach to the manubrium, ribs 2-7 attach to the sternal body, and rib 7 also attaches to the xiphoid process. These first 7 ribs are referred to as the true ribs because they are the only ones that attach directly to the sternal assembly. The false ribs, 8-10, attach to the costal cartilage of rib 7. The floating ribs (11-12) do not attach at all anteriorly and contain minimal costal cartilage. The ribcage serves to protect internal thoracic organs from injury. The compliant nature of costal cartilage allows for more flexibility in the ribcage and makes respiration easier [11].

Costal cartilage is a cylindrical hyaline cartilage composed of two component layers: a mid-substance (i.e., interstitial matrix) and the perichondrium. The interstitial matrix is a homogenous material located at the center of the cartilage. It is made up of collagens that are organized into

longer segments referred to as fibrils or fibers [12]. The network of interlaying collagen fibers contains proteoglycan monomers and link proteins formed by chondrocytes within a relatively large volume of water. The perichondrium envelops this matrix as the outer cartilaginous layer with two of its own distinct layers, one chondrogenic and one fibrous. The inner chondrogenic layer contains chondroblasts that allow it to grow and repair the interstitial matrix. This layer features both the network of collagen fibers from the interstitial matrix as well as a network made of transverse fibers that is continuous with the periphery of the matrix [13]. The fibrous connective tissue layer is the outermost layer, protecting the underlying cartilage and creating an interface that attaches to surrounding ligaments and interstitial muscles. It contains collagen fibers, blood vessels that provide blood supply to the underlying matrix, and fibroblasts [13].

The costal cartilage interstitial matrix undergoes two major structural changes with increasing age. The first of these is referred to within literature as the "amianthoid change" and occurs during all stages of life [14]. It is characterized by bundles of collagen fibers aligning parallel to the perichondrium layer and the depletion of glycosaminoglycans within proteoglycans in the interstitial matrix [14], [15]. These bundles of amianthoid fibers have been shown to be more brittle and rigid than the surrounding interstitial matrix [15]. This is likely because the realignment of the fibers turns the once isotropic interstitial matrix into an anisotropic material [16]. Collagen fibril diameter has also been found to increase with age in costal cartilage, even without obvious presence of amianthoid fibers. Proteoglycan diameter near the perichondrium remains relatively constant during the amianthoid change, resembling that of a newborn, and it is currently unclear how this change within the interstitial matrix influences the perichondrium [14]. The second major change experienced by the costal cartilage is the formation of calcifications with increasing age. There are two calcification patterns typically found in aging cartilage. The first is a more concentrated, globular calcification located in the center of the interstitial matrix. This is more commonly observed in post-menopausal females [17], [18]. The other is a peripheral, shell-like calcification that forms underneath the fibrous layer of the perichondrium [19], seen more frequently in older males [18]. These calcifications can begin to form around 35 years of age [20].

Multiple studies have been conducted to investigate the effect of calcifications on costal cartilage material properties. Forman and Kent developed finite element models for costal cartilage sections from five subjects and manipulated the amount of calcification to study its effect on structural

response [21]. They found that the stiffness of costal cartilage with calcification levels increased to 24% ranged from 2.3 – 3.8 times that of the originally modeled cartilage with 0% calcification. Wang et al. found that the presence of calcifications increased the Young's modulus by 30.06% and improved mechanical strength. Stress-strain curves showed that cartilage with calcifications had lower strain than non-calcified cartilage [22]. The researchers inferred that these material property changes balance each other out to present similar structural behavior between calcified and non-calcified costal cartilage, despite the increased brittleness of the calcified cartilage.

Hydration may also affect the material properties of aging cartilage. Venn studied the water content of human femoral head cartilage, an articular cartilage that shares some structural similarities with costal cartilage [23]. Older cartilage was shown to have decreased hydration levels and had formed pre-existing cracks, compared to more hydrated younger cartilage without the presence of any cracks. The differences noted by Venn indicate that material response changes with age in articular cartilage, and calls for investigation into that change in costal cartilage as well.

A number of studies have been conducted on the tensile material properties of the costal cartilage interstitial matrix, but none of them have investigated the perichondrium and most of them have limited subject demographics. Guo et al. conducted tensile tests on costal cartilage from donors aged 5-25 years old and found the strength, stress-strain relationship, relaxation, and creep of the material from 70 donors [24]. This study did not test samples to failure or investigate the properties of older cartilage. Nowinski conducted tensile tests on costal cartilage interstitial matrix samples from donors aged 10 to 59 years of age [25]. Samples were tested to failure at two loading rates and failure properties, elastic modulus, and strain energy density were calculated from every test. Interstitial matrix samples were found to show decreasing failure stress and strain values with increasing age at both loading rates. The quantification of these material properties, which account for the influence of donor age and loading rate, allows for further research to compare these properties with those of the other costal cartilage layers.

The compressive material properties of costal cartilage have been investigated more thoroughly; however, it has been shown that costal cartilage demonstrates a different material response in different loading conditions (i.e. tension vs. compression). Lau et al. conducted indentation stiffness tests on calcified and non-calcified interstitial matrix samples [19]. Nowinski conducted compression testing on cylindrical interstitial matrix samples and found differences in tensile and

compressive material properties [25]. Griffin et al. investigated the compressive properties of costal cartilage in patients with microtia [26]. Tripathy and Berger used atomic force microscopy indentation tests to determine compressive properties of the costal cartilage interstitial matrix [27]. Feng et al. studied the compressive material properties of costal cartilage in individuals with pectus excavatum [28].

Although the existing research on costal cartilage material properties primarily focuses on the interstitial matrix, there have been some studies that have investigated different aspects of the perichondrium. Costal cartilage is frequently used for reconstructive procedures such as rhinoplasties, and there are a few studies investigating the impact of incorporating the perichondrium layer into costal cartilage grafts [29], [30], [31], [32], [33], [34]. Shi et al. compared macroscopic and histological properties of cartilage grafts with and without the perichondrium and also performed compression tests on the grafts [30]. They found that the compressive elastic modulus of grafts without the perichondrium was smaller (8.68 ± 0.62 MPa) than that of those with the perichondrium retained (11.05 ± 1.28 MPa). Other perichondrium research has investigated the regenerative and healing properties of the material [35], [36], [37], [38], [39], [40].

Forman et al. studied the contribution of the perichondrium fibrous layer to the structural properties of the costal cartilage during bending [41]. Specimens were tested as an assembly composed of the sternum, costochondral junction, costal cartilage, and the anterior end of the rib bone. The samples were first subjected to loading with the perichondrium intact. Since the specimens were being tested multiple times, they were not loaded to failure. After a few perichondrium-intact tests, the fibrous layer of the perichondrium was removed and the tests were repeated. The results showed that removing the fibrous layer reduced the costal cartilage effective stiffness by 47%. This indicates that the perichondrium significantly influences the structural response of the costal cartilage and calls for additional research to be conducted on the layer's influence on material properties as well.

Gradischar et al. also studied the mechanical properties of whole costal cartilage sections [42]. Tensile tests were performed on costal cartilage sections at a strain rate of 0.0013 s^{-1} at a uniaxial load of up to 50 MPa. The only material property reported for these tensile tests was the elastic modulus, which was calculated for the region between 20 N and 40 N for each test with values ranging from 5.6 to 29.6 MPa. The role of the perichondrium layer was not investigated in this

study. This study is limited in that there were only two donors used, both older males (60 and 83 years old). While a range of rib levels were tested for each donor, the small sample size and restricted range of donor ages calls for more research on larger sample sizes with an investigation into the effects of age and sex.

Roy et al. performed three-point bending tests on porcine auricular and costal cartilage from 4-8 week old Yorkshire pigs [43]. Auricular cartilage was cut into strips with the perichondrium either preserved, removed from one side, or removed from both sides. It is unclear whether the costal cartilage interstitial matrix was tested with the perichondrium layer. They calculated the elastic modulus of the costal cartilage to be 7.06 MPa. Modulus values for auricular cartilage were higher for samples tested with the perichondrium side on the opposite side of the applied bending load than those tested with the bending force applied to the perichondrium side. Kohles conducted follow-up bending tests on porcine auricular and costal cartilage to determine the tensile and compressive elastic moduli [44]. They found that the costal cartilage elastic modulus in tension was 6.131 MPa, which is within 1 MPa of the bending modulus found by Roy et al [43].

Other types of cartilage contain a perichondrium layer as well, and studies have investigated the effect of the perichondrium on their material properties. All types of hyaline, articular, and elastic cartilage have a perichondrium. The nasal septum is made of hyaline cartilage and its material properties have also been studied in the context of reconstructive surgery. Tekke et al. investigated the contribution of the perichondrium to the material properties of nasal septum cartilage in bending [45]. Strips of nasal cartilage were prepared with and without the perichondrium and subjected to three-point bending. Samples with perichondrium were found to form more surface deformations before failure while those without the perichondrium acted more brittle, failing with less relative deformations. Greater modulus of elasticity, bending strength, and deflection were obtained from perichondrium-containing samples compared to those without. This study used a sample size of 14 samples per category and the role of donor age was not taken into consideration.

Another type of cartilage known to contain a perichondrium layer is elastic cartilage. Elastic cartilage contains more elastic fibers than costal cartilage and is designed to hold a specific shape rather than to be load-bearing. Sun et al. investigated the role of the perichondrium in rabbit auricular cartilage on its material properties in tension and compression [46]. They conducted stress-relaxation tests on 12 auricular cartilage samples from six-year-old Japanese white rabbits.

Tests were run at a loading rate of 10 mm/min. Interestingly, the researchers found the samples with the perichondrium intact reached the same stress value of 2.5 MPa while experiencing just over half of the strain that was experienced by the samples with the perichondrium removed. It is unclear how this influences the failure properties of auricular cartilage perichondrium but those tests with the perichondrium had a greater modulus (33.08 MPa) than those without the perichondrium (25.37 MPa). Removal of the perichondrium reduced auricular cartilage stiffness by 23%.

The existing literature provides further motivation for research into the role of the perichondrium on costal cartilage material properties. There is limited work investigating the role of the perichondrium on material and structural response of human costal cartilage, with still little known about the effect of the perichondrium on material properties of other human and mammal cartilages. Many existing studies are limited to the elastic modulus of various cartilages, creating a gap in the knowledge regarding other material properties, such as ultimate and failure stress and strain, and strain energy density. Most of the literature only investigates material properties at a single loading rate as well, creating uncertainty in the influence of loading rate on cartilage material properties. None of the existing cartilage research investigated the isolated perichondrium layer, demonstrating the need for further research to quantify its material properties.

Human body models (HBMs) have been used to predict human injury tolerance and response to various real-world loading scenarios and are frequently used by vehicle manufacturers. These models incorporate existing structural and material property data for different regions of the body. Currently available virtual human body models include the Global Human Body Models Consortium (GHBMC) HBMs [47], SAFER HBMs [48], VIVA+ HBMs [49], and the Total Human Model for Safety (THUMS), developed by Toyota Motor Corporation and Toyota Central Research and Development [50]. These models are currently used in the evaluation of existing and novel vehicle safety features to assess their contributions to injury mitigation [51], [52], [53], [54], [55]. To accurately predict injury, the models rely on accurate material properties and geometries. As a result, these models are continuously being improved and validated with updated tissue properties and muscle activation. Focusing on the thorax, material property data have been collected for human rib bone and costal cartilage interstitial matrix for a range of ages, but not the costal cartilage perichondrium [25], [56], [57], [58], [59]. Models of the thorax that incorporate these

thoracic material property data have shown improvements in model response [60], [61], [62]. Due to the limited existing research on the material property data of the costal cartilage, it is currently approximated as a homogenous substance, which does not represent its true cellular architecture or material properties. It is well-known that the different layers of the costal cartilage have inherently different material compositions, indicating that each layer would have unique material properties. The simplification of these human body models limits their ability to accurately simulate the response of the thorax to injurious loads.

Research Objectives

In order address the gap in knowledge of the influence of the perichondrium layer on the properties of the human costal cartilage, a research study was conducted to investigate the material properties of human costal cartilage perichondrium in tension. These data will improve the knowledge of the perichondrium layer and how the material properties of the costal cartilage change with respect to the different cartilage layers. These data will also improve the accuracy of human body models used to predict human injury tolerance in MVCs. Based on the literature regarding the material properties of other skeletal thoracic tissue and cartilage, it is hypothesized that the perichondrium will have higher material property values than the interstitial matrix, the material property values will decline significantly with increasing age, and the material property values with be unaffected by loading rate and donor sex. Therefore, the research objectives of this thesis are as follows:

1. Develop novel methods to fabricate and test human costal cartilage perichondrium samples in tension
2. Quantify the tensile material properties of costal cartilage perichondrium
3. Investigate the effect of cartilage layer on costal cartilage material properties

Methods

Fifty-six (n=56) costal cartilage perichondrium samples containing the fibrous layer and chondrogenic layer (i.e., two-layered samples) were fabricated from thirty-three (n=33) donors (Male [M]=19, Female [F]=14) aged from 11 to 69 years of age (Avg. 40.9 ± 16.7 yrs.). Thirteen (n=13) samples with the chondrogenic layer and no fibrous layer (i.e., one-layered samples) were fabricated from eight (n=8) donors (M=5, F=3) aged from 11 to 54 years of age (Avg. 35.5 ± 15.4 yrs.). All cartilage was obtained ethically from the Ohio State Body Donor Program and Lifeline of Ohio. All donors tested negative for bone disease. Costal cartilage was wrapped in saline-soaked gauze and stored at -20°C prior to sample fabrication. The costal cartilage was kept hydrated with normal saline throughout the fabrication process.

To fabricate tension coupons, some cartilage sections were clamped into a surgical costal cartilage graft slicer (AP-WCC, Anthony Products, Inc., Indianapolis, IN) and manually cut in half (Figure 1), while other cartilage slices were taken from the untested perichondrium of tissue previously used for interstitial matrix testing [25]. The extraneous soft tissue was then removed from each section to help visualize the fibrous layer and check for prior damage to the perichondrium that would exclude the sample from material testing. After large sections of soft tissue were cut off with a scalpel, the remaining soft tissue was removed with scissors. One-layered samples then had the fibrous layer removed with sandpaper (Figure 2).

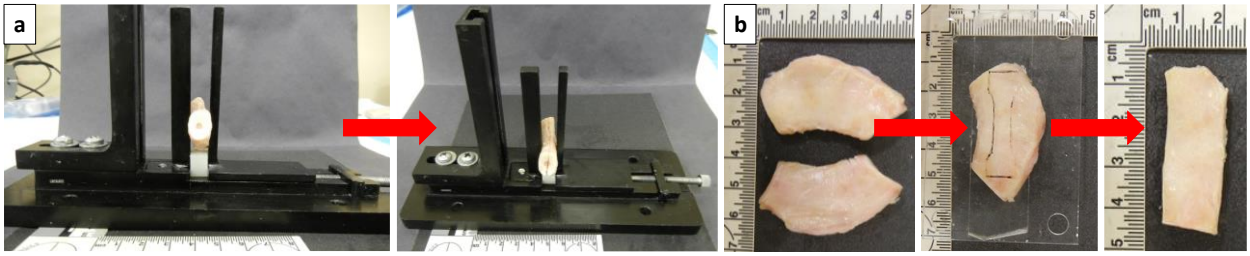

Figure 1. (a) Costal cartilage was sliced in surgical graft cartilage slicer (b) and was cut down to match sample dimensions.

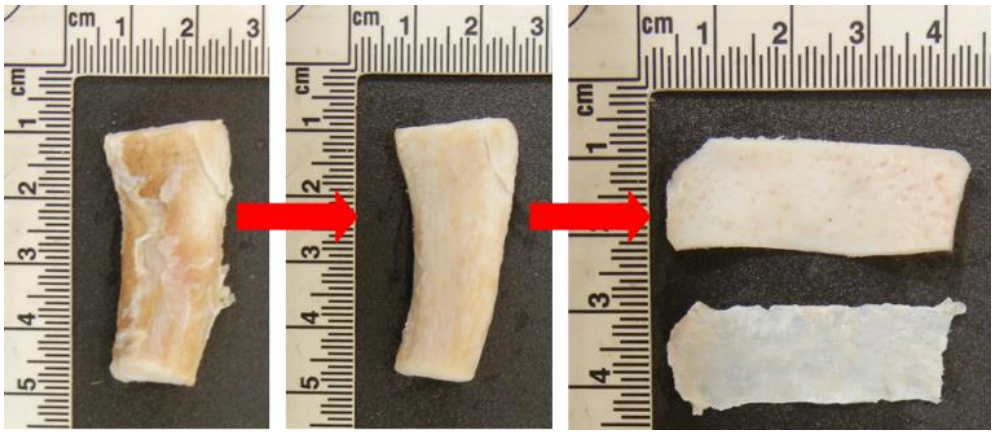

Figure 2. Extraneous soft tissue removed (left and middle) for all samples, fibrous layer removed for one-layered samples (right).

The interstitial matrix was next removed using curved wood chisels and 60 grit sandpaper. Since the costal cartilage is cylindrical, the perichondrium layer is naturally curved. Therefore, the curved wood chisels were chosen to match the perichondrium curvature and ensure uniform sample thickness. During interstitial matrix removal, samples were placed in one of two rectangular pockets within a large plastic block to hold the cartilage section and prevent sliding that would damage, loosen, or detach the fiber layer (Figure 3). The end of the cartilage was pressed against the wall of the pocket while the chisel was pushed and gently twisted to remove large amounts of interstitial matrix. The remaining interstitial matrix was removed using 60 grit sandpaper. The sandpaper was wrapped around various sizes of Allen wrenches to target areas of interstitial matrix with different curvatures and to smooth the surface of the chondrogenic layer. Sanding continued until the interstitial matrix was removed, the sample was less than 2 mm in thickness, the thickness was approximately uniform, and the sample could be pressed flat without incurring damage (i.e., cracks).

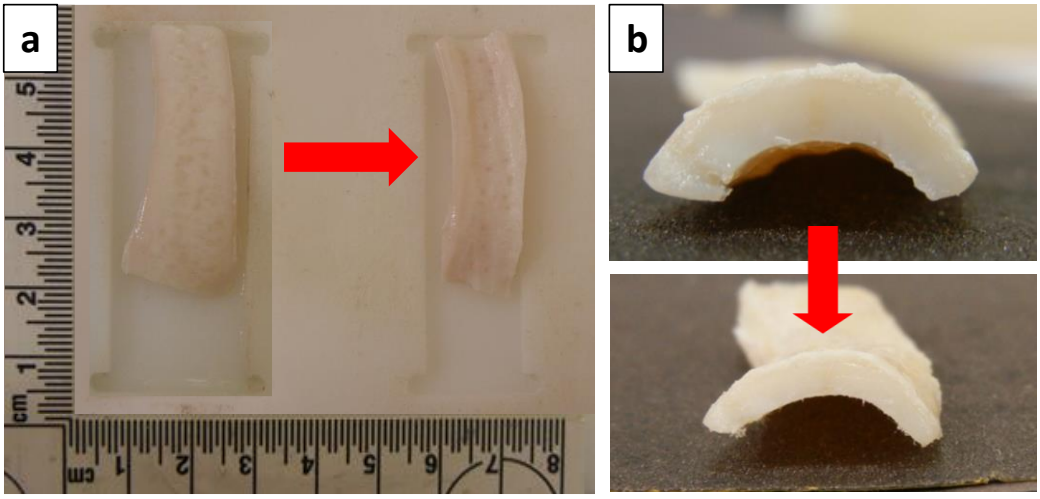

Figure 3. (a) The interstitial matrix was removed with wood chisels (b) and sandpaper.

The cartilage was then positioned on a custom stamping block, fibrous side up, using a plastic guide marked with the coupon outline, which was aligned with a custom-made stamp. The stamp was then used to cut a dog-bone shaped coupon (Figure 4). The coupon was inspected once more for soft tissue, and any that remained was removed.

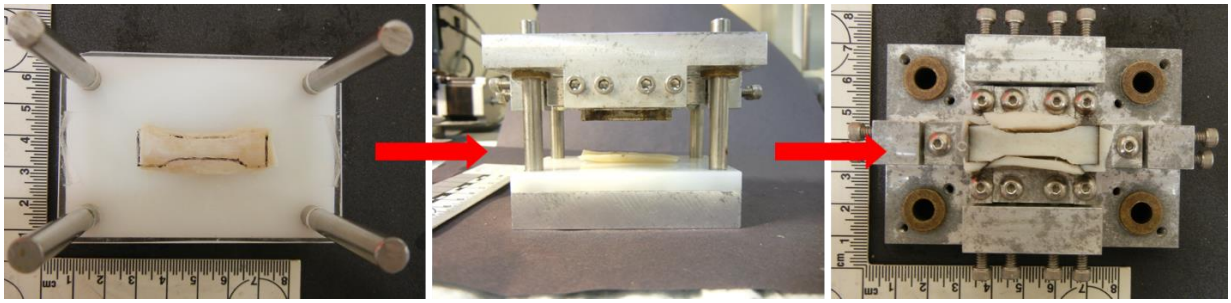

Figure 4. Costal cartilage perichondrium was stamped into a dog-bone shaped coupon.

The stamped coupon was then placed in a custom sanding jig. The outer corners and ends of the coupon grip areas were secured to the sanding jig with a small dot of super glue to prevent slipping and tapering during sanding (Figure 5). The sanding jig was placed on a base lined with sandpaper and the coupon was sanded down to its final thickness (Figure 6). The depth of the sanding jig pocket corresponded to the target coupon thickness. The depth of the pocket was either 1.13 mm or 1.3 mm for the one-layered and two-layered samples, respectively.

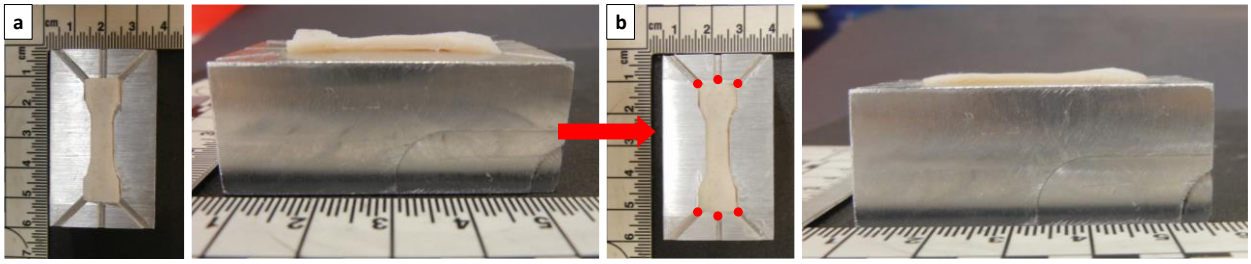

Figure 5. (a) Coupon in the sanding jig without superglue from the top and side view. (b) Coupon secured in the sanding jig with superglue from the top and side view. Glue placement is marked by the red dots.

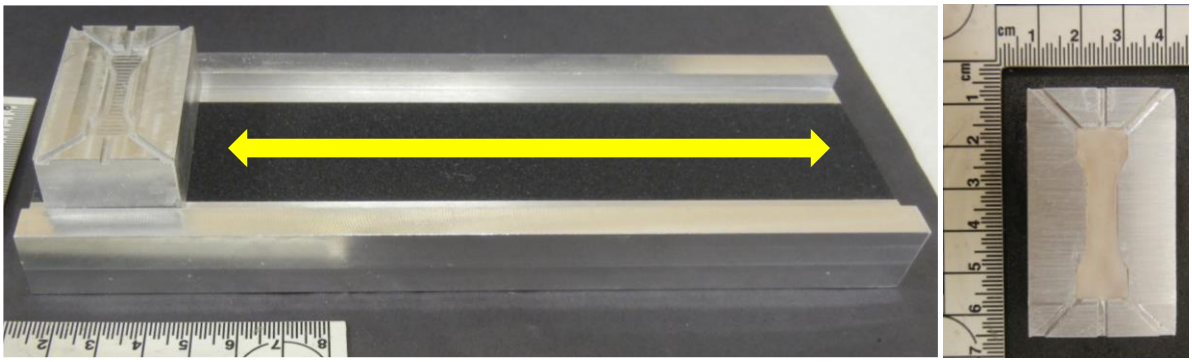

Figure 6. Sanding assembly with sanding direction marked in yellow (left) and sanding jig with sanded cartilage coupon (right).

The coupon was removed from the sanding jig using toothpicks and the superglue was carefully peeled off of the coupon with a scalpel. The entire sample was checked for uniform thickness with force-limiting calipers. Any imperfections were manually corrected using 220 grit wet sandpaper. The width and thickness of the gage length were measured with digital low force calipers (IP54, MICROTECH, Kharkiv, Ukraine) at a maximum force of 0.8 N. Two-layered samples had a gage width ranging from 5.38 mm to 7.02 mm (Avg. 6.03 ± 0.27 mm) and gage thickness between 0.97 mm and 1.39 mm (Avg. 1.22 ± 0.11 mm). One-layered sample width ranged from 5.59 mm to 6.46 mm (Avg. 6.04 ± 0.28 mm) and thickness ranged from 0.56 mm to 1.30 mm (Avg. 0.98 ± 0.23 mm). Finished samples (Figure 7) were placed on a precision scale (AR0640, OHAUS, Parsippany, NJ) to measure the mass before testing.

Some of the cartilage from donors aged 40 years and older and most of the cartilage from donors older than 50 years of age had pre-existing cracks in the interstitial matrix (Figure 8a). These cracks

made sample fabrication difficult. In some cases, these cracks reached the inner chondrogenic layer and either made the tissue untestable or led to a sample with pre-existing cracks. In most cases, these pre-existing cracks in the chondrogenic layer were not visible (Figure 8b) until the test was already in progress and the tensile load was actively applied to the sample (Figure 8c). This resulted in these pre-existing cracks being featured in the chondrogenic layer of samples made from older donors. This means that the chondrogenic layer already contained cracks before any testing load was even applied to the sample.

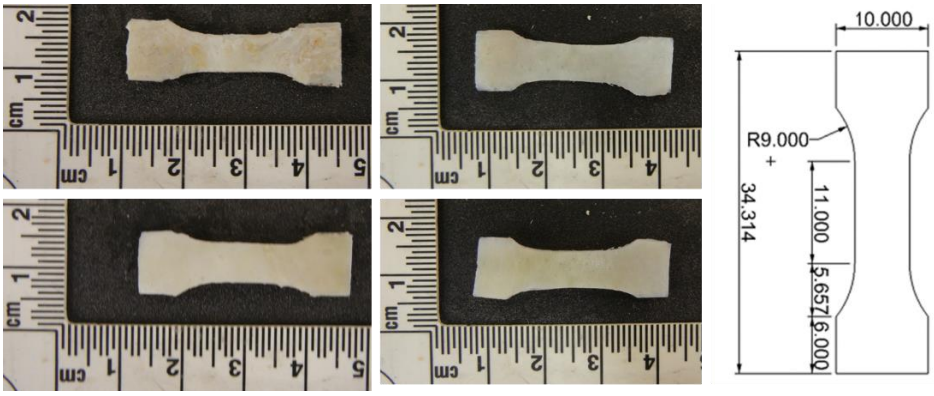

Figure 7. Left to right: two-layered sample (fibrous side on top, chondrogenic side on bottom), one-layered sample, and sample dimensions.

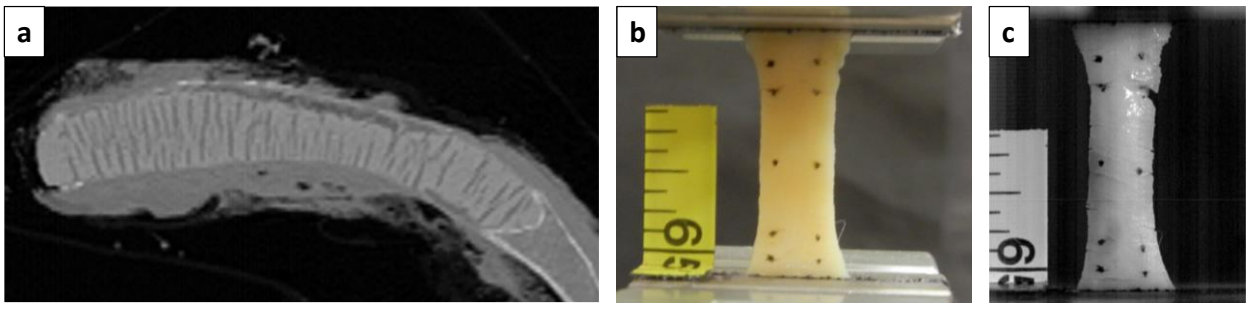

Figure 8. (a) CT scan of the costal cartilage showing pre-existing cracks in the interstitial matrix. (b) Perichondrium sample with pre-existing cracks in the test setup before loading. (c) The same sample in the test setup during loading, with visible pre-existing cracks.

Sample gage lengths were marked with a pattern of ten dots using black India ink on the face from which the interstitial matrix was removed. Samples were then secured to the material testing system (800LE4, Test Resources Inc., Shakopee, MN) with pneumatic grips (G229-0.5-8 Pneumatic Grip, Test Resources, Shakopee, MN) (Figures 9-10). Before placement into the test

setup, the grip pressure was adjusted based on the donor age (Table 1). The grip pressures were optimized to hold the samples while reducing incidences of sample failures next to grips and incidences of samples slipping in the grips during the test. An alignment jig was used to place, center, and align the sample in the grips. The sample was clamped into the top grip first, then any bowing in the gage length was reduced by applying gentle pressure with tweezers to the outer arc, if necessary, while the bottom grip was clamped (Figure 10). A preload of approximately 0.25 N was then applied to remove slack before testing. Samples were then loaded to failure at either a fast (0.5 s^{-1}) or slow (0.005 s^{-1}) target strain rate (Figure 11).

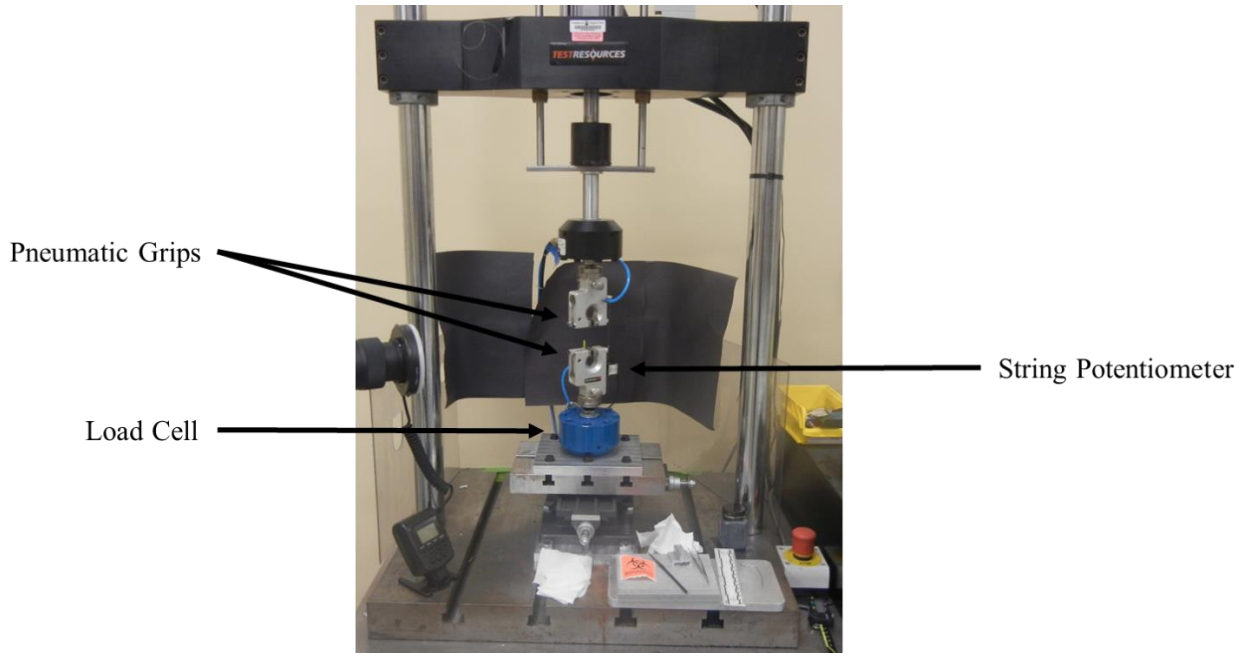

Figure 9. Tensile test setup on material testing system.

Table 1. Pneumatic grip pressure applied to perichondrium samples by donor age.

Age (years)	Grip Pressure (psi)
10s	47-50
20-35	45-47
36-45	40
46+	35

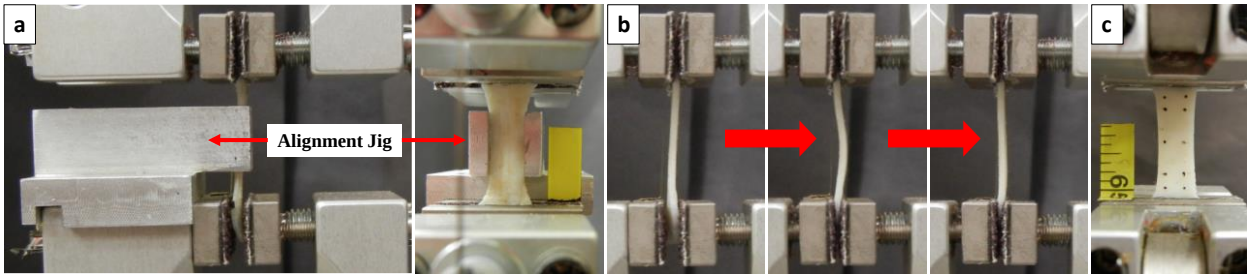

Figure 10. (a) Sample was placed into the tensile test setup using an alignment jig. (b) The sample was secured into the test setup one grip at a time and a 0.25 N preload was applied. (c) The final perichondrium sample secured with the pneumatic grips.

Video data were collected using a high-speed video camera (Phantom v9.1m, Vision Research, Wayne, NJ) with an additional lens (Tokina atx-i 100mm F2.8 FF MACRO, Kenko Tokina Co., Ltd, Tokyo, Japan), a pixel resolution ranging from 27.6 to 29.2 pixels/mm, and a bit depth of 8 bits/pixel. Videos for 0.005 s^{-1} target loading rate tests had a frame rate of 50 fps and videos for 0.5 s^{-1} target loading rate tests had a frame rate of 2000 fps. A ring light (LD-RF-550D, Shenzhen ZLY Technology Co., Ltd, China) was positioned around the camera lens and a high frequency fluorescent light was aimed at the sample during testing to provide consistent and direct lighting in the video. The material testing system was equipped with a reaction load cell (1210ACK-300-B, Interface, Scottsdale, AZ) below the bottom grip and a string potentiometer (150-0121, Firstmark Controls, Creedmoor, NC) for data collection. Grip-to-grip displacement and force data were collected from the string potentiometer and load cell, respectively. Potentiometer and load cell data were collected at a rate of 20,000 Hz. The dot pattern on the samples was tracked using TEMA motion analysis software (TEMA Motion 3D, Image Systems Inc., Linköping, Sweden) to collect displacement of the sample within the gage length.

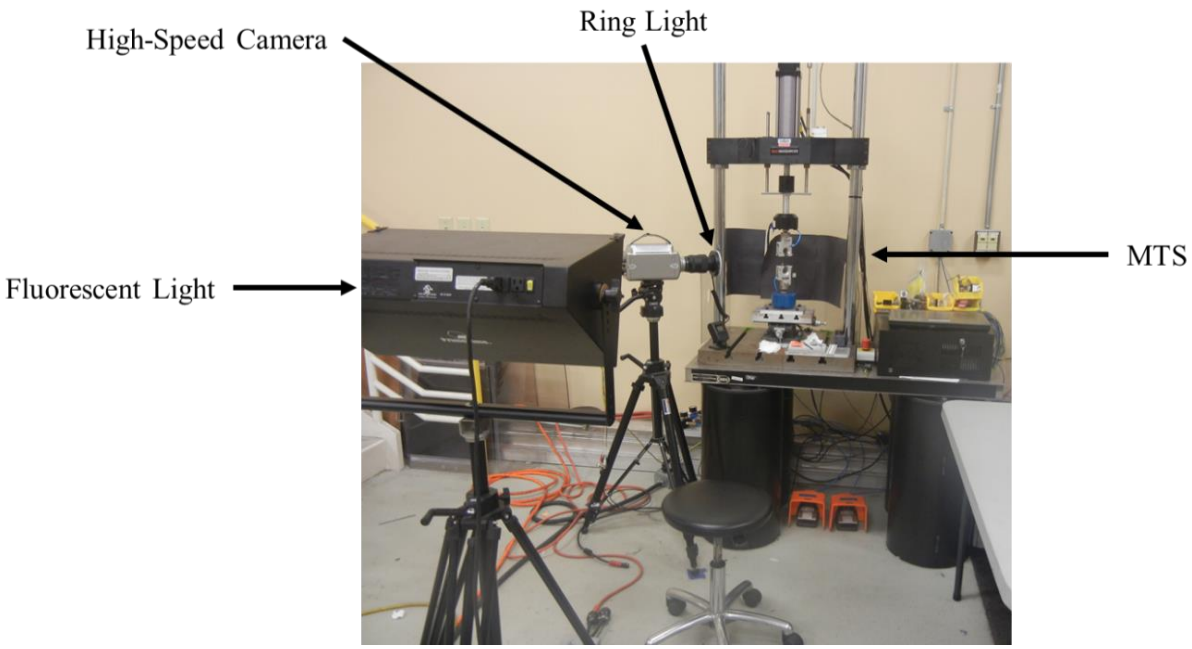

Figure 11. Testing setup showing high-speed camera and light sources.

The sample failure point was determined as the first data point just before a large drop in the force curve and when a visible failure occurred in the video. Prior to filtering, force and displacement data were truncated at the point of failure. The data were then mirrored and reflected across this point to prevent biasing of the failure point during filtering. Data collected at the 0.5 s^{-1} target loading rate were filtered with a pseudo SAE CFC 50 Hz filter [63]. Data from the 0.005 s^{-1} target loading rate were filtered using a 1-25 Hz band stop filter. Filtered force data were down sampled to match the sampling rate of the video data and were truncated at the failure point. Axial engineering strain was calculated using the vertical positions of the top and bottom dot pairs for each test. Engineering stress was calculated from the force and gage dimensions. Strain energy density (SED) was calculated as the area under the stress-strain curve. Elastic modulus was determined using the slope of a linear region in the stress-strain curve bounded by percentages of the maximum stress value (i.e., 35% maximum stress to 70% maximum stress). Some donors had multiple successful tests for one sample type at the same loading rate. The material property values for these tests were averaged and only one value was reported for the donor for that sample type and loading rate. Donors with averaged material property values are listed in the Appendix (Table A1).

Statistical analyses were performed to investigate the roles of age, sex, loading rate, pre-existing cracks, and failure layer on the material properties. The alpha (α) value was set to 0.05 to determine the significance of all analyses. A Shapiro-Wilk test (W) was used to assess the normality of all material property distributions for two- (Table A2) and one-layered samples (Table A3). An analysis of variance (ANOVA) was used to investigate the roles of age, sex, the interaction of age and sex, the presence of pre-existing cracks, and the layer of the sample that failed first on the tensile material properties of two-layered samples at each loading rate. Data collected from one donor for both loading rates within one sample type or within both sample types at one loading rate are referred to as matched loading rate data and matched sample type data, respectively, because a matched pair existed that enabled a direct comparison between loading rates or sample types within a donor. Wilcoxon signed rank tests (S) were run on 16 matched pairs to evaluate the effect of loading rate for two-layered samples, four matched pairs to evaluate the effect of sample type for 0.005 s^{-1} tests, and seven matched pairs to evaluate the effect of sample type for 0.5 s^{-1} tests. The Spearman's rank correlation coefficient (ρ) was also determined for all material properties with respect to age for each loading rate to account for nonlinear trends because some distributions were not found to be normal in the Shapiro-Wilk test. The significance of the correlation was tested using a Student's t-test.

Results

Twenty-six (n=26) successful two-layered tests from twenty-one (n=21) donors and five (n=5) successful one-layered tests from four (n=4) donors were completed at the 0.005 s^{-1} target loading rate. Thirty (n=30) successful two-layered tests from twenty-seven (n=27) donors and eight (n=8) successful one-layered tests from seven (n=7) donors were done at the 0.5 s^{-1} target loading rate. For cases where multiple successful tests were completed for a donor within a particular loading rate and sample type, the material properties were averaged across tests to obtain a singular value for each donor. The average slow strain rate for two-layered samples was 0.0037 s^{-1}, and 0.0046 s^{-1} for one-layered samples. The average fast loading rate was 0.3412 s^{-1} for two-layered samples, and 0.4392 s^{-1} for one-layered samples. The failure and ultimate points were very similar on average because they were often the same point. Sixteen (n=16) two-layered samples failed at the

fibrous layer and eight (n=8) failed at the chondrogenic layer at the 0.005 s^{-1} target loading rate. Twenty-two (n=22) two-layered samples failed at the fibrous layer and seven (n=7) failed at the chondrogenic layer at the 0.5 s^{-1} target loading rate.

Final material property data for two-layered samples are reported in Table 2. The effect of various factors on the material properties of two-layered samples was investigated with an ANOVA test (Tables 3-4). At the 0.005 s^{-1} target loading rate, donor age and the interaction of donor age and sex was found to have a significant effect on the elastic modulus, ultimate stress, failure stress, and SED. Sex, the presence of pre-existing cracks, and the layer of the sample that failed first did not significantly influence any material properties. At the 0.5 s^{-1} target loading rate, donor age was found to significantly influence the elastic modulus, ultimate stress and strain, failure stress and strain, and SED for two-layered samples. Further investigation showed low correlation with age among samples that failed at the chondrogenic layer first as opposed to a strong correlation with age among samples that failed first at the fibrous layer at the 0.5 s^{-1} target loading rate. The interaction of age and sex only significantly affected the ultimate strain, but caution should be taken with this statistic as the majority of older samples at this loading rate were females. Sex and the presence of pre-existing cracks did not significantly affect the material properties at the 0.5 s^{-1} loading rate. The ultimate strain and failure strain were found to be significantly affected by the failure layer of the samples. The strain values of samples that failed in the chondrogenic layer tended to be on the lower end relative to samples that failed in the fibrous layer at the 0.5 s^{-1} target loading rate (Figures 12-13). Bar charts comparing strain average values show that there is a more visible difference in material property values between failure layers at the 0.5 s^{-1} target loading rate, while not much difference is noted at the 0.005 s^{-1} target loading rate (Figure 14).

Table 2. Final material property averages and standard deviations for all two-layered samples.

Material Property	0.005 s^{-1}		0.5 s^{-1}	
	Average	Standard Deviation	Average	Standard Deviation
Modulus	0.1034	0.0716	0.1105	0.0602
Ultimate Stress	8.9719	6.2918	10.4418	7.5652
Ultimate Strain	0.1269	0.0262	0.1285	0.0312

Failure Stress	8.6307	6.0229	10.4166	7.5801
Failure Strain	0.1319	0.0247	0.1304	0.0309
SED	0.5471	0.3819	0.6685	0.5981

Table 3. ANOVA results (p-values) for all two-layered samples tested at 0.005 s^{-1}. Significant values are bold.

Material Property	Age	Sex	Age * Sex	Pre-existing Cracks	Failure Layer
	p-value	p-value	p-value	p-value	p-value
Modulus	**0.0005**	0.1757	**0.0029**	0.8001	0.2533
Ultimate Stress	**<.0001**	0.3325	**0.0041**	0.4681	0.3069
Ultimate Strain	0.0779	0.6827	0.8088	0.4174	0.8337
Failure Stress	**<.0001**	0.3894	**0.0067**	0.4503	0.3018
Failure Strain	0.1099	0.4397	0.9052	0.6577	0.6464
SED	**0.0002**	0.7631	**0.0269**	0.5976	0.3418

Table 4. ANOVA results (p-values) for all two-layered samples tested at 0.5 s^{-1}. Significant values are bold.

Material Property	Age	Sex	Age * Sex	Pre-existing Cracks	Failure Layer
	p-value	p-value	p-value	p-value	p-value
Modulus	**0.0399**	0.9005	0.5287	0.8391	0.2438
Ultimate Stress	**0.0015**	0.6289	0.1903	0.67	0.8704
Ultimate Strain	**0.0006**	0.1761	**0.0498**	0.4395	**0.0097**
Failure Stress	**0.0014**	0.6336	0.1887	0.6746	0.8575
Failure Strain	**0.0028**	0.1827	0.0769	0.5711	**0.0095**
SED	**0.0006**	0.7339	0.0766	0.3339	0.7229

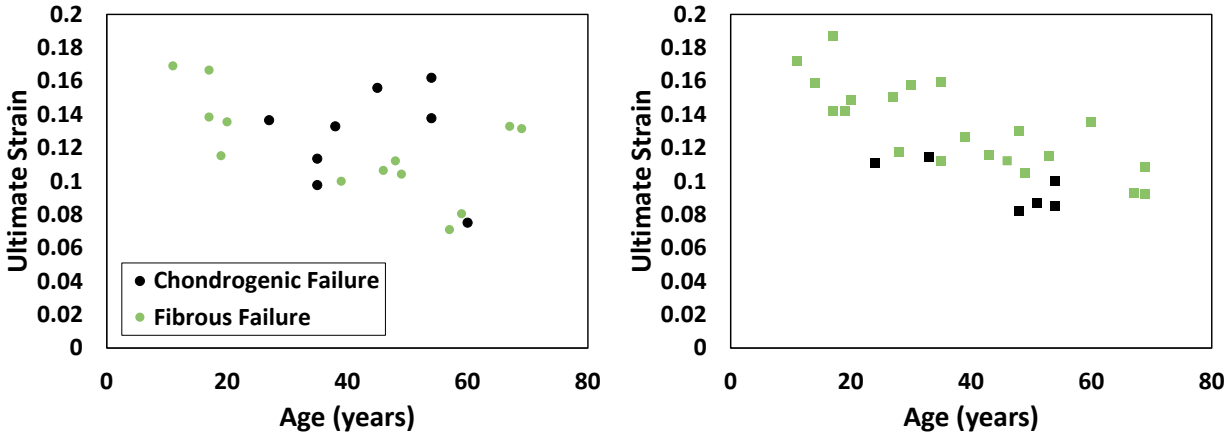

Figure 12. Ultimate strain vs. age for two-layered samples separated by the layer that failed first at the 0.005 s^{-1} target loading rate (left) and 0.5 s^{-1} target loading rate (right).

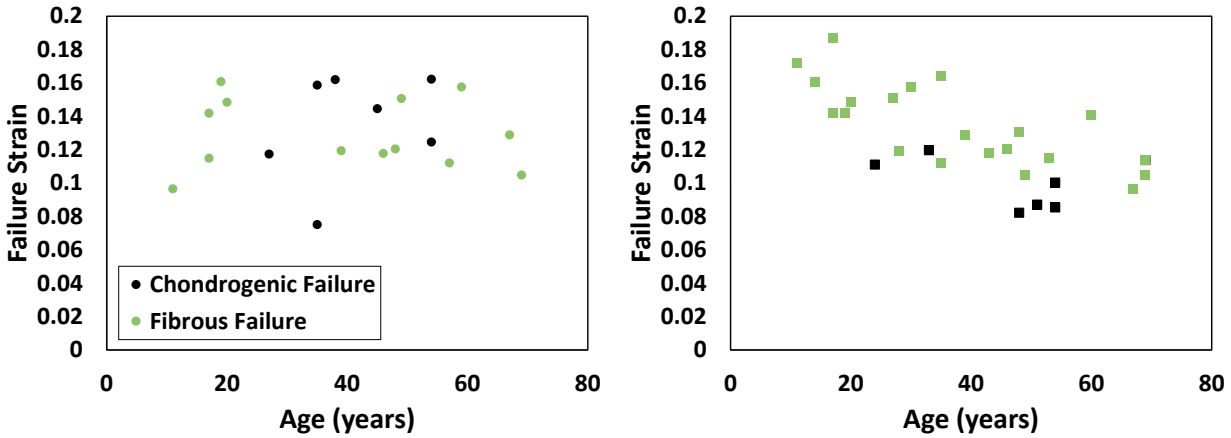

Figure 13. Failure strain vs. age for two-layered samples separated by the layer that failed first at the 0.005 s^{-1} target loading rate (left) and 0.5 s^{-1} target loading rate (right).

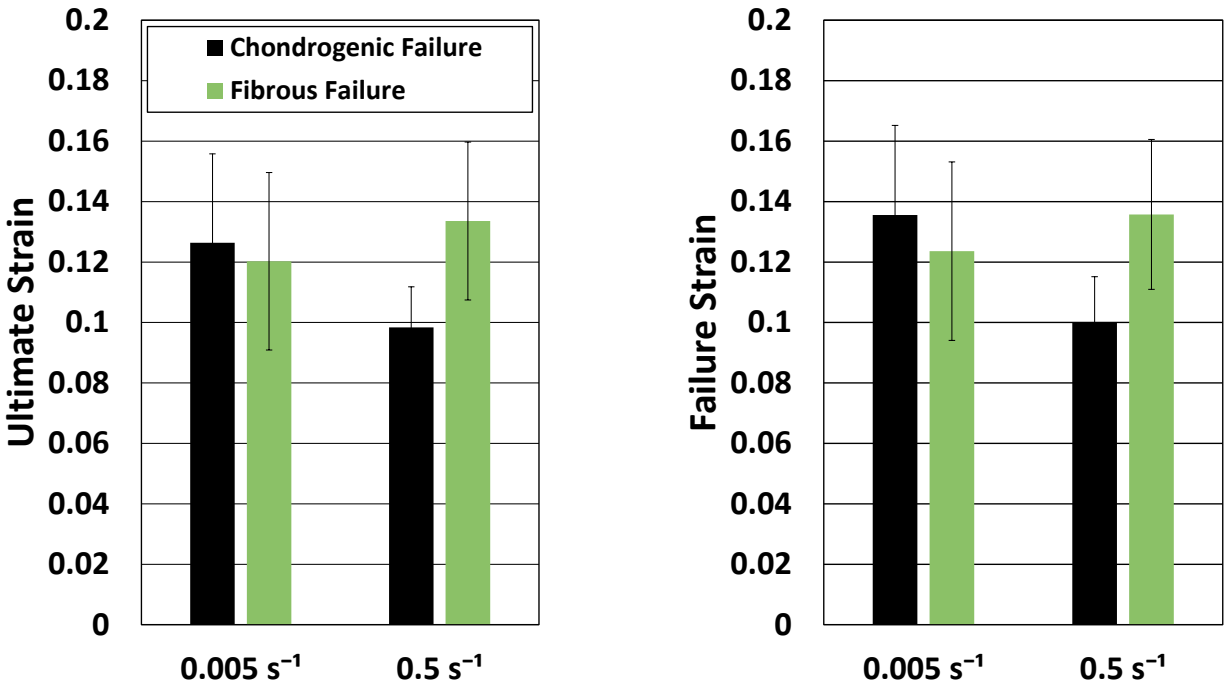

Figure 14. Average strain values for each failure layer are shown at the 0.005 s^{-1} and 0.5 s^{-1} loading rates.

To further investigate the influence of age on material properties, the Spearman's rank correlation coefficient was calculated for two-layered samples at each loading rate (Table 5). Increasing donor age resulted in a significant decrease in the elastic modulus, ultimate stress, failure stress, and SED at the 0.005 s^{-1} target loading rate and ultimate stress and strain, failure stress and strain, and SED at the 0.5 s^{-1} target loading rate. To aid in visualization of these age trends as well as shed light on the lack of influence of sex, material property values for each test were plotted against age and color-coded by sex (Figures 15-20). Linear trend lines were added to aid in the visualization of two-layered sample age trends without the influence of sex. Other types of trend line fits and their R^2 values can be seen in the Appendix (Figures 33-38, Tables A4-A9). Overall, a quadratic curve was found to have the largest R^2 values for all material properties at the 0.5 s^{-1} target loading rate and for all properties at the 0.005 s^{-1} target loading rate except for the modulus and stresses, for which an exponential curve had the largest R^2 values.

Table 5. Spearman's rank correlation coefficient (ρ) and associated p-values for all two-layered samples at both loading rates.

Material Property	0.005 s^{-1}		0.5 s^{-1}	
	ρ	p-value	ρ	p-value
Modulus	-0.7225	**0.0007**	-0.4186	0.0838
Ultimate Stress	-0.7783	**0.0001**	-0.7018	**0.0012**
Ultimate Strain	-0.2656	0.2867	-0.5995	**0.0086**
Failure Stress	-0.7762	**0.0002**	-0.7018	**0.0012**
Failure Strain	-0.186	0.4598	-0.5798	**0.0117**
SED	-0.7556	**0.0003**	-0.7928	**<.0001**

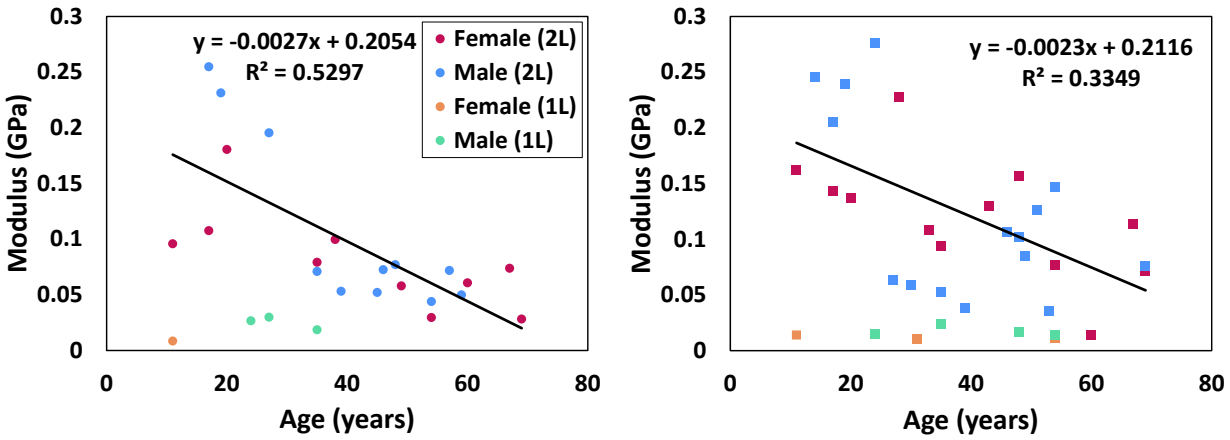

Figure 15. Elastic modulus vs. age delineated by sample layer type and sex, with the 0.005 s^{-1} target loading rate on the left and 0.5 s^{-1} on the right. The linear trend lines encompass all two-layered samples, independent of sex.

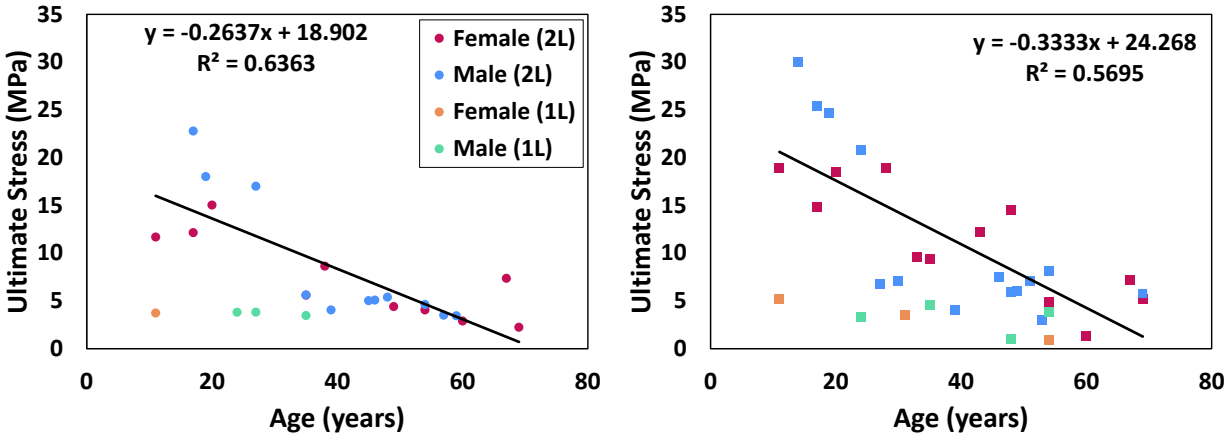

Figure 16. Ultimate stress vs. age delineated by sample layer type and sex, with the 0.005 s^{-1} target loading rate on the left and 0.5 s^{-1} on the right. The linear trend lines encompass all two-layered samples, independent of sex.

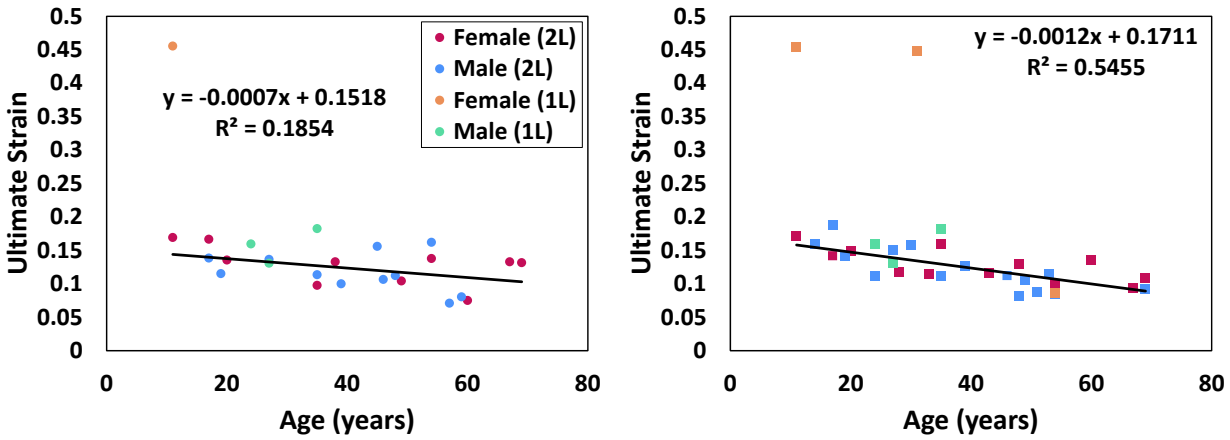

Figure 17. Ultimate strain vs. age delineated by sample layer type and sex, with the 0.005 s^{-1} target loading rate on the left and 0.5 s^{-1} on the right. The linear trend lines encompass all two-layered samples, independent of sex.

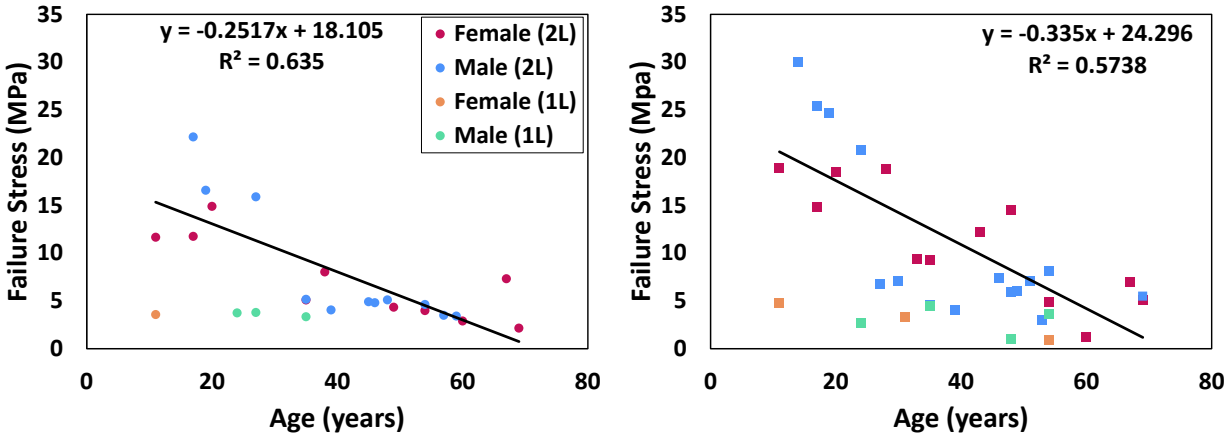

Figure 18. Failure stress vs. age delineated by sample layer type and sex, with the 0.005 s^{-1} target loading rate on the left and 0.5 s^{-1} on the right. he linear trend lines encompass all two-layered samples, independent of sex.

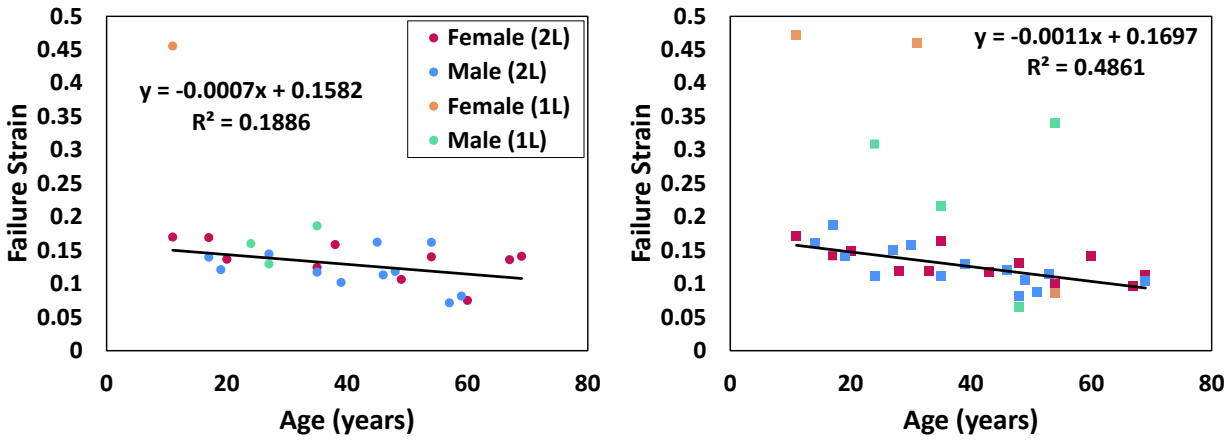

Figure 19. Failure strain vs. age delineated by sample layer type and sex, with the 0.005 s^{-1} target loading rate on the left and 0.5 s^{-1} on the right. The linear trend lines encompass all two-layered samples, independent of sex.

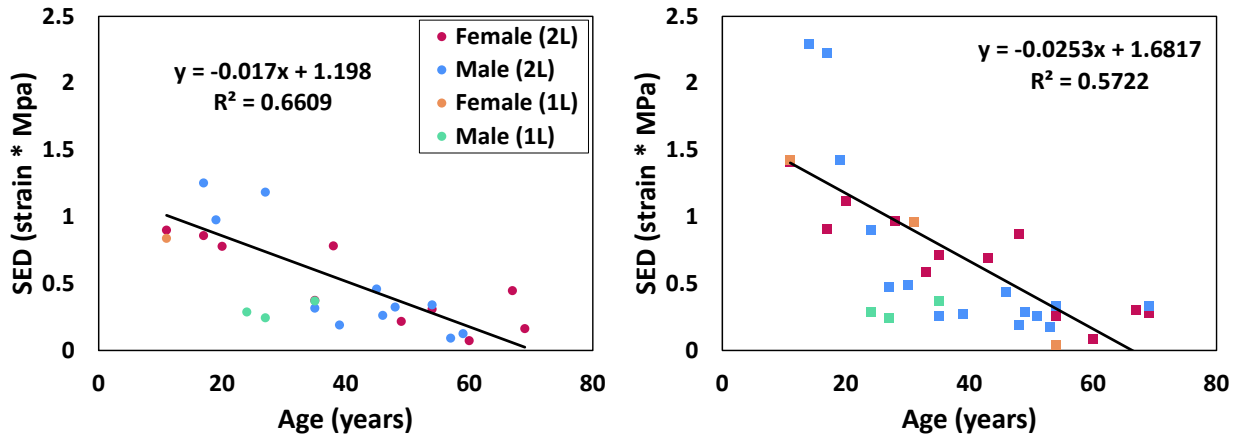

Figure 20. SED vs. age delineated by sample layer type and sex, with the 0.005 s^{-1} target loading rate on the left and 0.5 s^{-1} on the right. The linear trend lines encompass all two-layered samples, independent of sex.

A Wilcoxon signed rank analysis was conducted on matched loading rate data from sixteen (n=16) donors aged 11-69 years of age (Avg. 38.625 ± 19) to investigate the role of loading rate on material properties (Table 6). Loading rate only significantly affected the ultimate and failure stress of two-layered samples. This was reflected in the stress-strain curves, which showed the 0.5 s^{-1} target loading rate tests reaching higher stress values than the 0.005 s^{-1} target loading rate tests (Figure 21). Average material property values were compared with bar charts in Figure 22.

Table 6. Wilcoxon signed rank results for the significance of loading rate on material properties of two-layered samples.

Material Property	Wilcoxon Signed Rank	
	S	p-value
Modulus	-11.5	0.5016
Ultimate Stress	-31.5	**0.0494**
Ultimate Strain	-3.5	0.8552
Failure Stress	-32.5	**0.0419**
Failure Strain	2.5	0.9032
SED	-22.5	0.1726

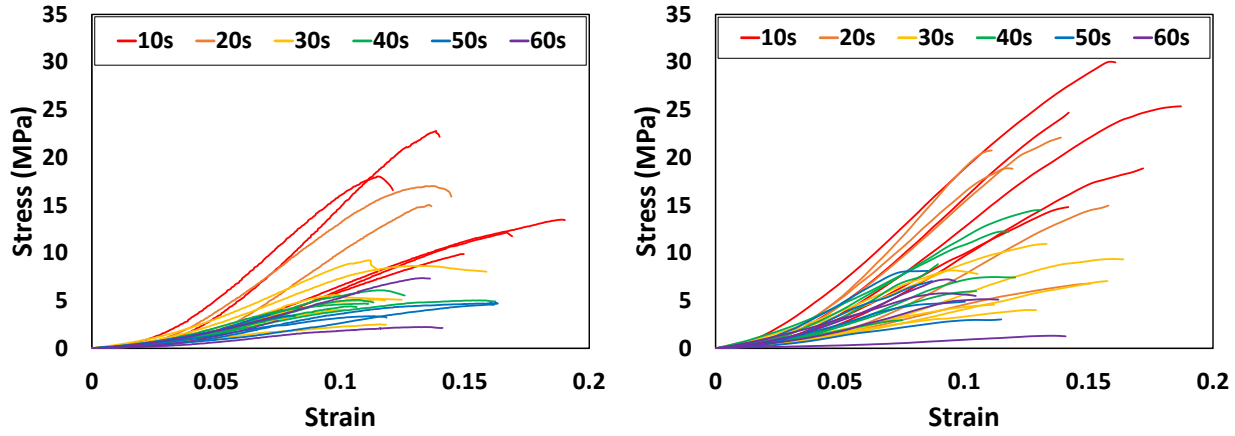

Figure 21. Stress-strain curves of all two-layered samples are plotted by decade, with the 0.005 s^{-1} loading rate on the left and the 0.5 s^{-1} loading rate on the right.

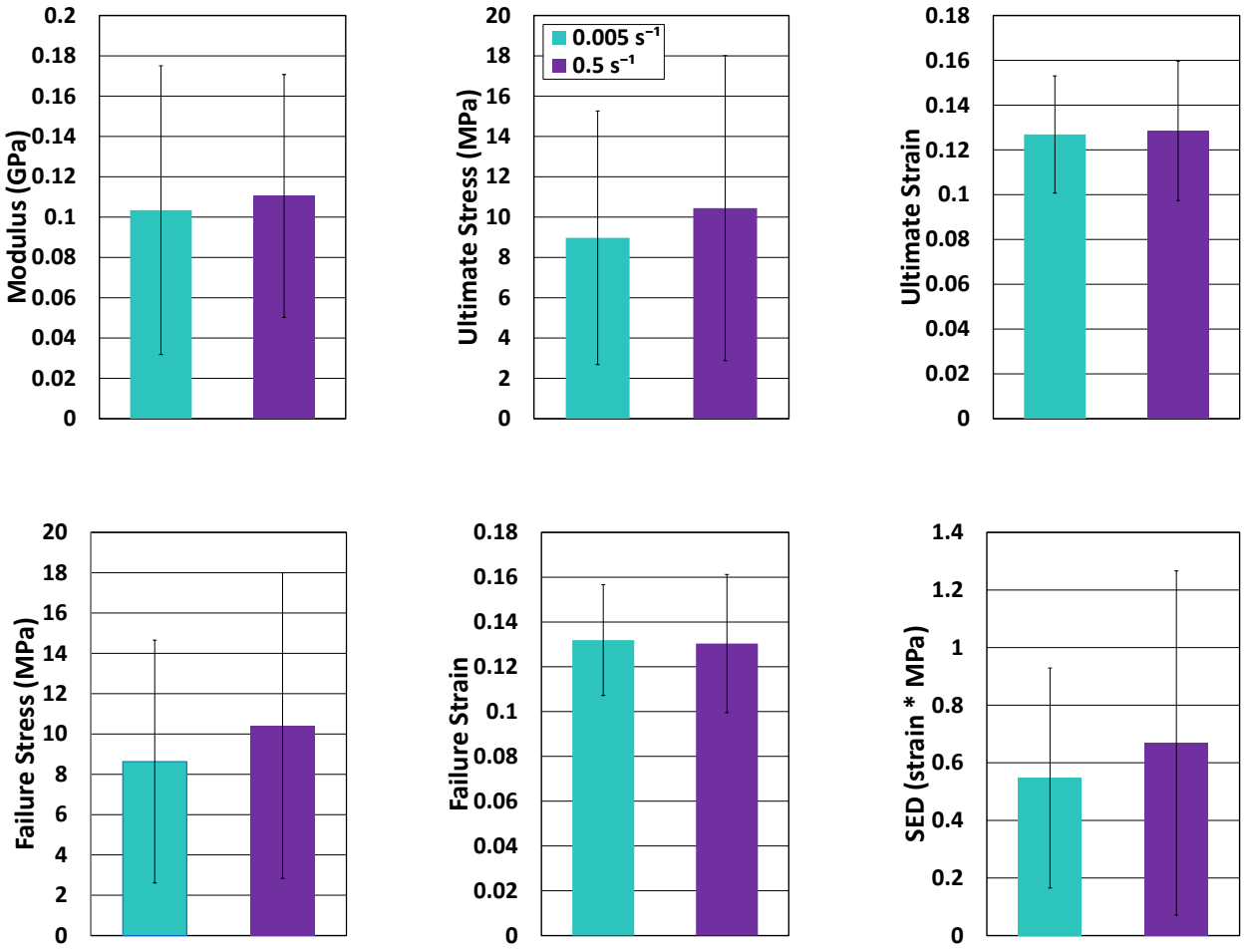

Figure 22. Material property averages and standard deviations for matched loading rate data for two-layered samples tested at 0.005 s^{-1} and 0.5 s^{-1}.

Samples from older donors were more likely to possess pre-existing cracks. Neither of the ANOVAs performed at the 0.005 s^{-1} (Table 3) and 0.5 s^{-1} (Table 4) target loading rates found statistical significance regarding the presence of pre-existing cracks on any material properties. Scatter plots (Figures 23-28) show the trends in material property values for samples with and without pre-existing cracks to be similar. Material property trends with age may be different for samples with pre-existing cracks, but they holistically fit in with the age trends of samples without pre-existing cracks.

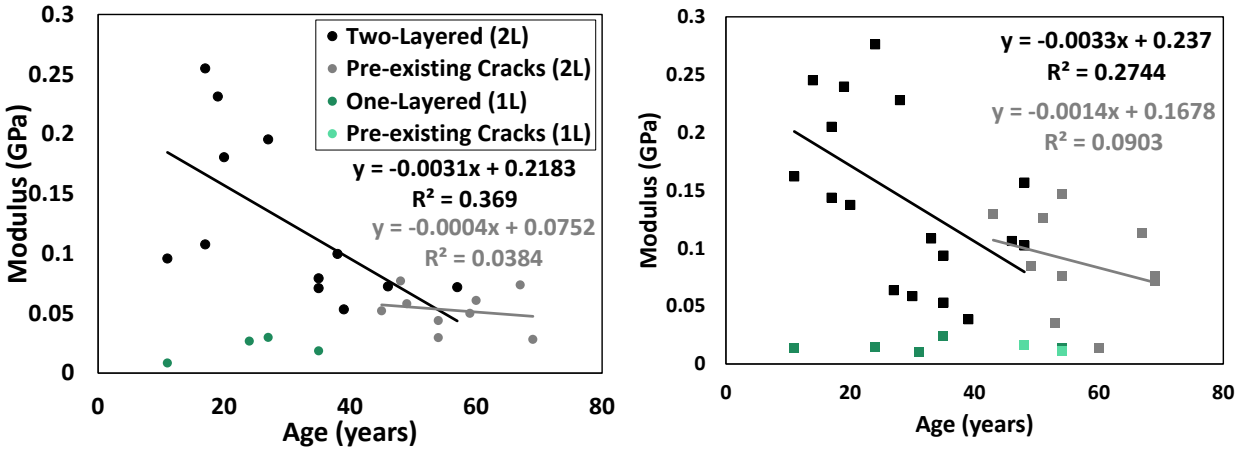

Figure 23. Elastic modulus vs. age for all samples, delineated by sample layer type and the presence of pre-existing cracks, with the 0.005 s^{-1} loading rate on the left and 0.5 s^{-1} loading rate on the right.

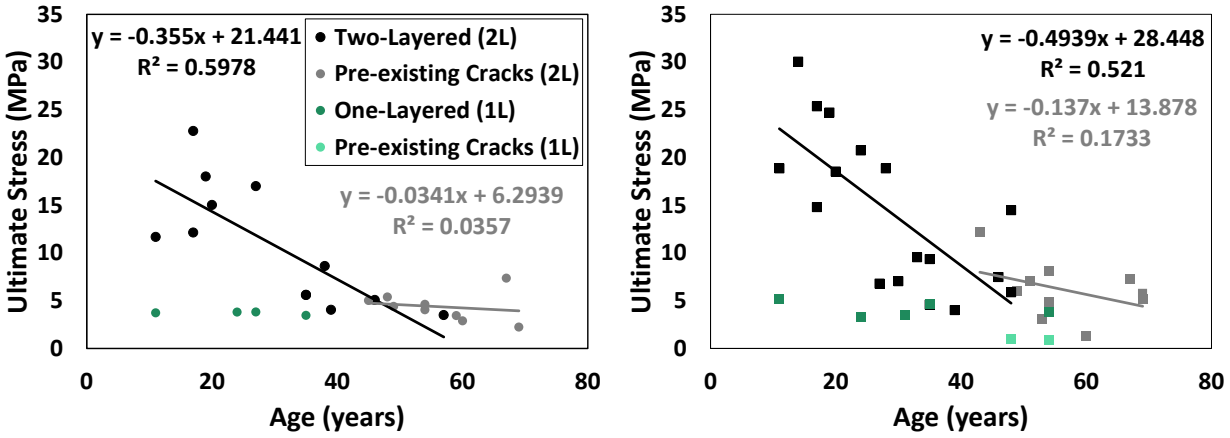

Figure 24. Ultimate stress vs. age for all samples, delineated by sample layer type and the presence of pre-existing cracks, with the 0.005 s^{-1} loading rate on the left and 0.5 s^{-1} loading rate on the right.

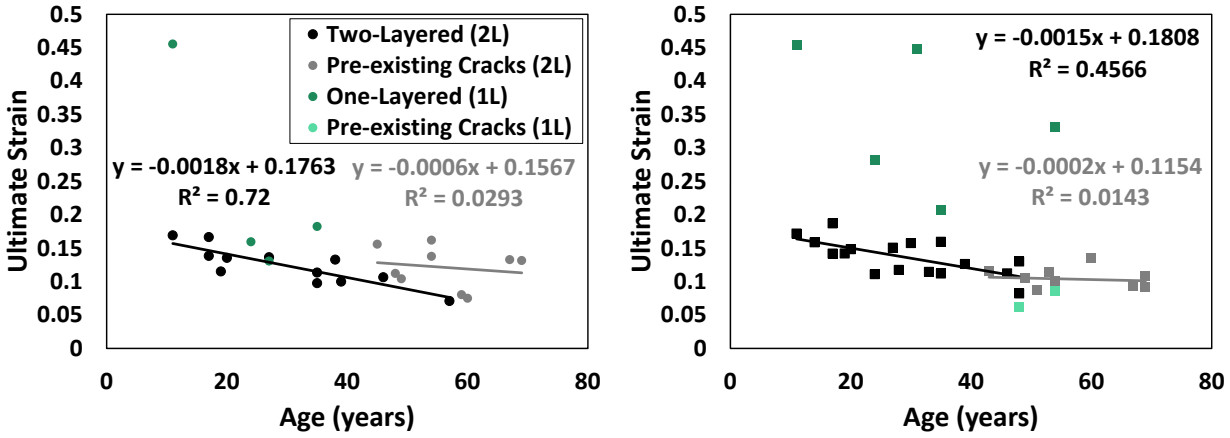

Figure 25. Ultimate strain vs. age for all samples, delineated by sample layer type and the presence of pre-existing cracks, with the 0.005 s^{-1} loading rate on the left and 0.5 s^{-1} loading rate on the right.

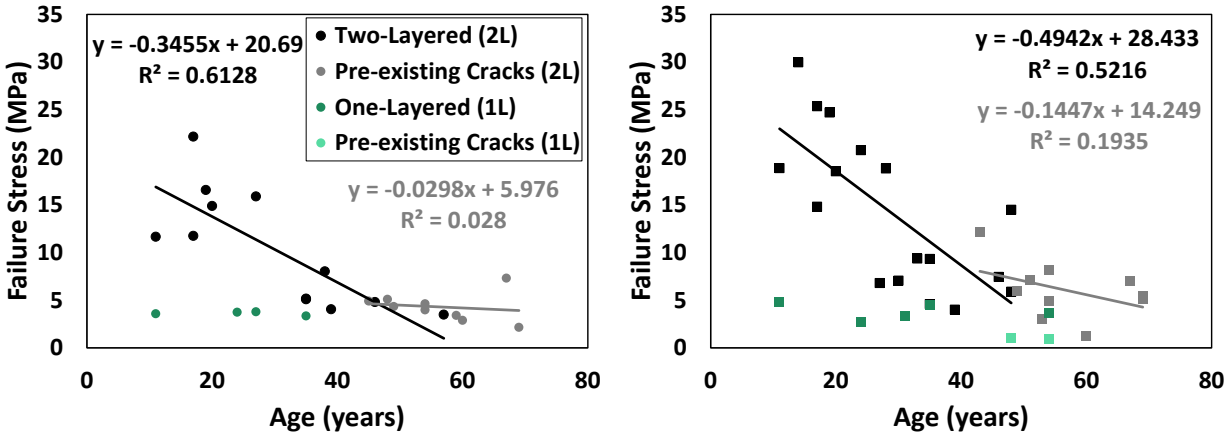

Figure 26. Failure stress vs. age for all samples, delineated by sample layer type and the presence of pre-existing cracks, with the 0.005 s^{-1} loading rate on the left and 0.5 s^{-1} loading rate on the right.

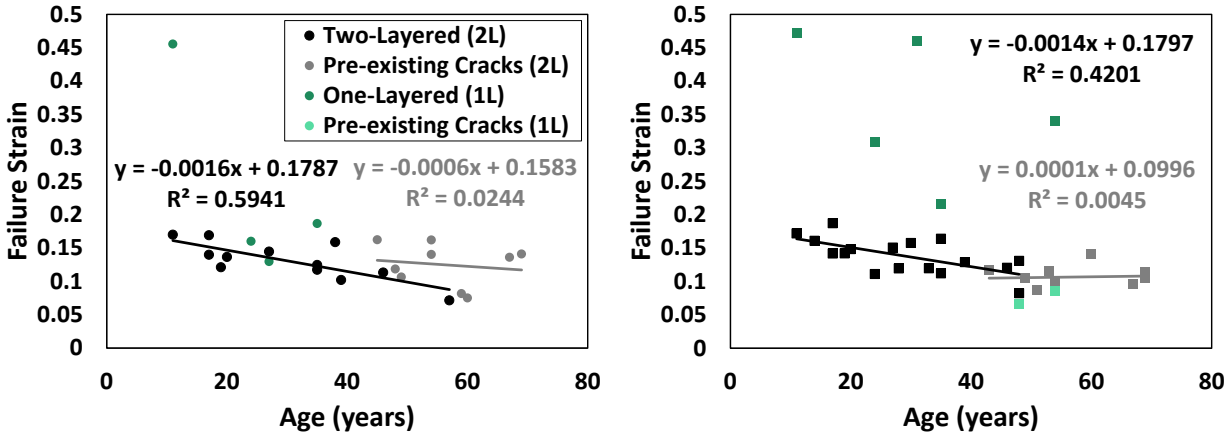

Figure 27. Failure strain vs. age for all samples, delineated by sample layer type and the presence of pre-existing cracks, with the 0.005 s^{-1} loading rate on the left and 0.5 s^{-1} loading rate on the right.

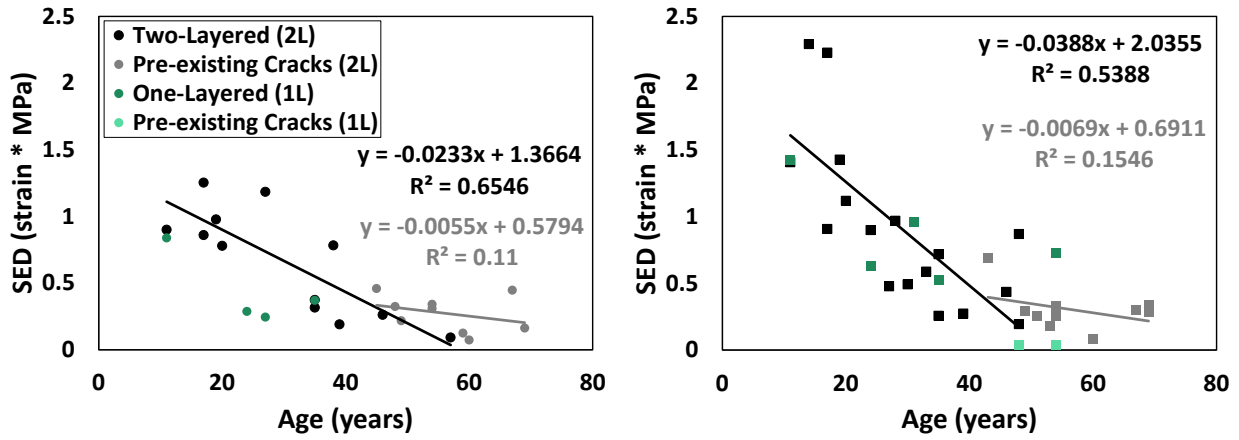

Figure 28. SED vs. age for all samples, delineated by sample layer type and the presence of pre-existing cracks, with the 0.005 s^{-1} loading rate on the left and 0.5 s^{-1} loading rate on the right.

Fewer analyses were performed for one-layered samples due to the smaller sample size. Additionally, the one-layered sample population was biased towards younger subjects and had fewer donors than that of the two-layered samples. Matched loading rate data were only obtained from three (n=3) donors aged 11-35 years of age (Avg. 23.3 ± 12) so matched statistical analyses were not possible. Final material property values for the one-layered samples for all subjects are shown in Table 7. Material property averages appear to be generally similar between loading rates, with differences visible in the stresses and SED average values (Figure 29). One-layered sample material properties do not appear to display the same age trends as those of two-layered samples.

Table 7. Final material property averages and standard deviations for all one-layered samples at both loading rates.

Material Property	0.005 s^{-1}		0.5 s^{-1}	
	Average	Standard Deviation	Average	Standard Deviation
Modulus	0.0179	0.0177	0.0091	0.0056
Ultimate Stress	3.6725	0.1803	4.3655	0.9520
Ultimate Strain	0.2658	0.1646	0.3138	0.1265
Failure Stress	3.5514	0.1983	3.9734	1.1518
Failure Strain	0.2674	0.1634	0.3326	0.1297

SED	0.4989	0.2974	0.8578	0.4911

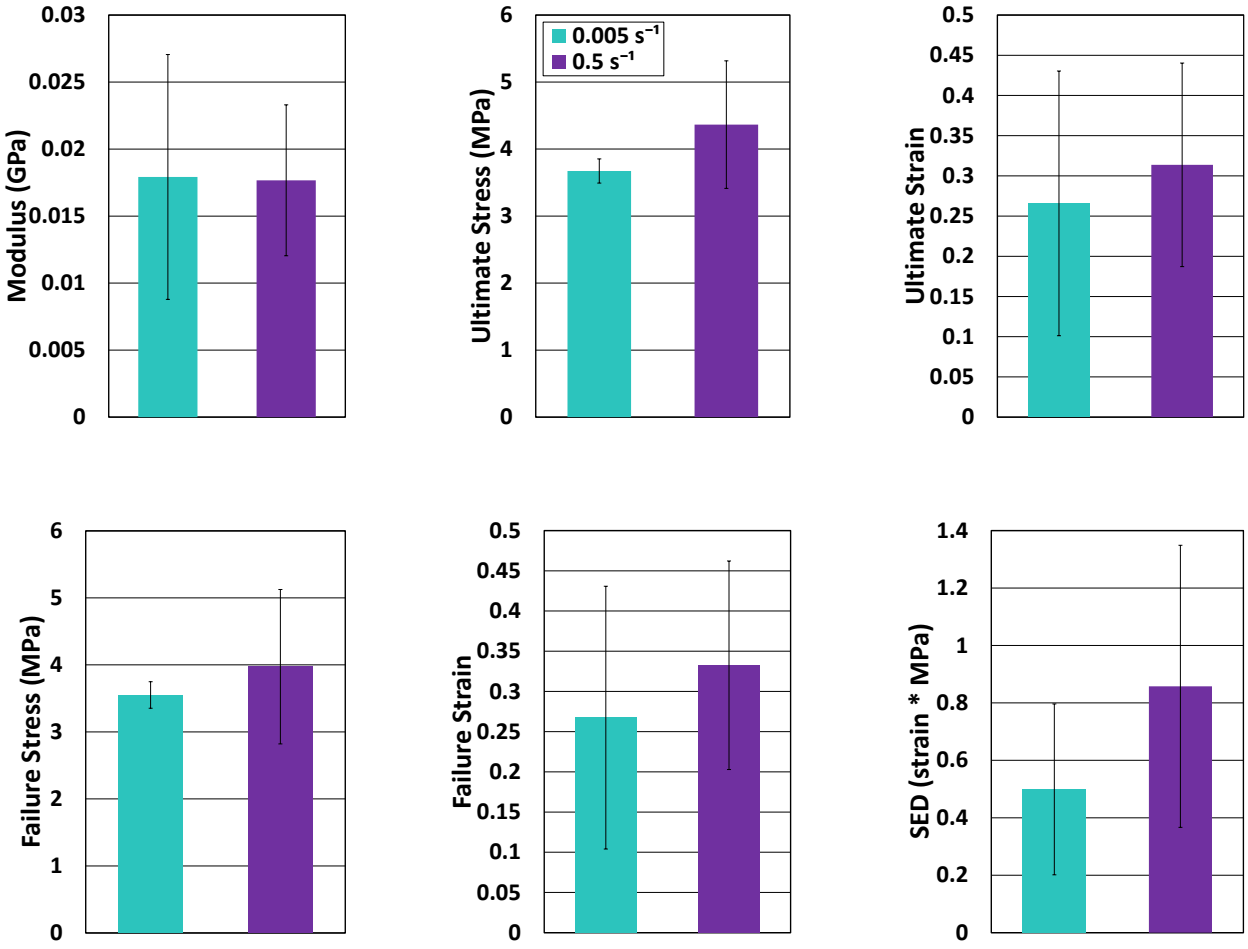

Figure 29. Material property averages and standard deviations for matched loading rate data from one-layered samples tested at 0.005 s^{-1} and 0.5 s^{-1}.

The role of sample type on matched material property values at each loading rate was investigated with a Wilcoxon signed rank analysis (Table 8). Matched sample type data were obtained for the 0.005 s^{-1} target loading rate from three (n=3) donors aged 11-35 years of age (Avg. 24.3 ± 12.2) and for the 0.5 s^{-1} target loading rate from six (n=6) donors aged 11-54 years of age (Avg. 37.7 ± 17.6). To maximize the sample size of the analysis, an additional pair was included at each loading rate. This pair was composed of a one-layered sample and a two-layered sample of the same sex and similar age. The 0.005 s^{-1} target loading rate analysis, then, used four (n=4) matched pairs from five (n=5) donors aged 11-35 years of age (Avg. 23.8 ± 10.0) and the 0.5 s^{-1} target loading

rate analysis used seven (n=7) matched pairs from eight (n=8) donors aged 11-54 years of age (Avg. 36.9 ± 16.2). None of the differences between sample types were statistically significant at the slow loading rate, and only modulus and failure stress showed significance due to sample type. This is likely due to the small number of matched pairs. Despite this, material properties of the one-layered samples appear to strongly differ from those of the two-layered samples. Stress, strain, and modulus show particularly strong differences between sample types. Overall, two-layered samples had a greater failure stress and one-layered samples had a greater failure strain for each loading rate (Figures 30-31).

Table 8. Wilcoxon signed rank results for the significance of sample type on matched sample type material property data at each loading rate.

Material Property	Wilcoxon Signed Rank			
	0.005 s^{-1}		0.5 s^{-1}	
	S	p-value	S	p-value
Modulus	-5	0.1250	-10.5	**0.0313**
Failure Stress	-5	0.1250	-10.5	**0.0313**
Failure Strain	4	0.2500	9.5	0.0625
SED	-4	0.2500	4.5	0.4375

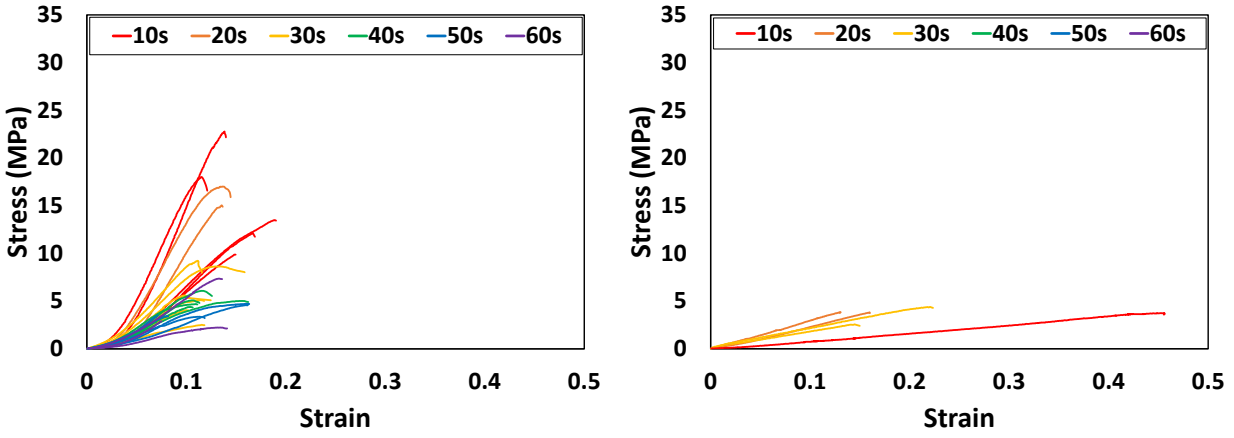

Figure 30. Stress-strain curves for two-layered (left) and one-layered (right) samples at 0.005 s^{-1}.

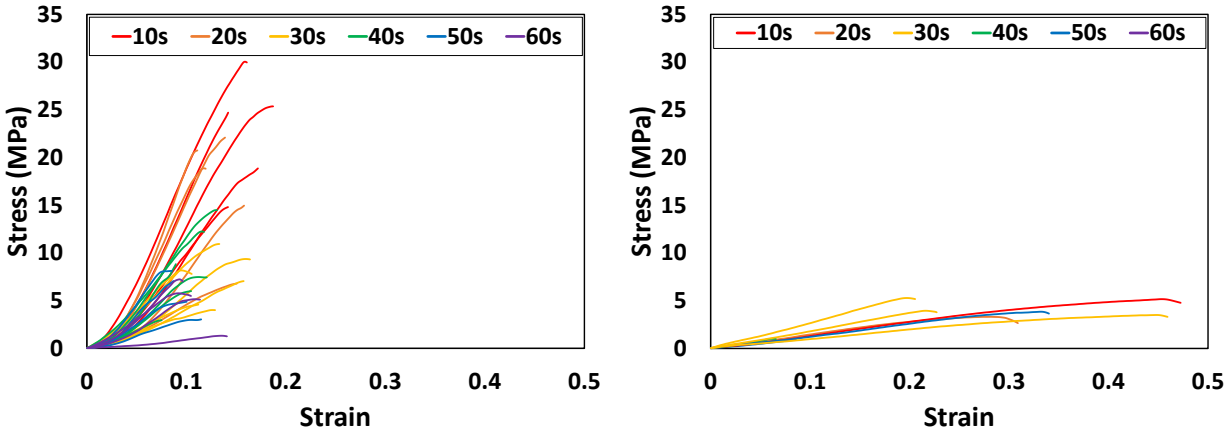

Figure 31. Stress-strain curves for two-layered (left) and one-layered (right) samples at 0.5 s^{-1}.

Discussion

This study investigated the roles of age, sex, loading rate, pre-existing cracks, and failure layer on the tensile material properties of human costal cartilage perichondrium. No significant effect of sex was found for any of the material properties investigated in this study. This is supported by existing costal cartilage research [25]. The effect of loading rate on the material properties was only found to be statistically significant for the ultimate and failure stress of two-layered samples. The p-values for the ultimate and failure stresses from the Wilcoxon signed rank analysis of matched loading rate data were significant, but still relatively close to the α value of 0.05. Other studies on the influence of loading rate on costal cartilage material properties have not found statistical significance of loading rate on any of the properties they investigated. Nowinski tested interstitial matrix samples at the same target loading rates as the current study and found that no material properties were significantly affected by loading rate [25]. However, there could also be differences in loading rate dependency between the interstitial matrix and perichondrium due to differences in material composition and structure.

In the current study, most material properties were found to decrease with increasing donor age. Some perichondrium samples were made from cartilage that contained the internal calcification patterns described in Stewart and McCormick and Rejtarová et al. [17], [18], but none were made

from cartilage with the peripheral calcifications observed by Rejtarová et al. and Lau et al. [18], [19]. Therefore, the change in material properties with age in this study are likely due to the amianthoid change and decreased hydration levels. Previous research on the interstitial matrix of costal cartilage observed changes in material properties with increasing age, lending support to the finding that costal cartilage perichondrium properties change with age. Nowinski also found significance in donor age with respect to the ultimate stress, ultimate strain, and strain energy density for costal cartilage interstitial matrix at two loading rates [25]. Studies on the central and peripheral layers of other types of cartilage have also observed material property changes with aging in both layers. Elliot et al. conducted tensile testing on the peripheral and middle zones of human patellar cartilage from 10 subjects to determine linear region (elastic) modulus [64]. They found that samples from donors less than 70 years of age had an average modulus of 23.92 ± 12.29 MPa and samples from donors aged older than 70 years had an average modulus value of 4.27 ± 2.89 MPa. Within the surface zone, the modulus of elasticity was found to decrease significantly in subjects older than 70 years of age. This means that the surface zone of patellar cartilage became stiffer with increasing age. Kempson et al. conducted tensile testing on human femoral and talus cartilage, both of which are articular cartilage [65]. Similar to the findings of the current study, they found the fracture stress for both superficial and mid-depth cartilage to significantly decrease with age.

Two-layered samples failed either in the fibrous layer or the chondrogenic layer first. Of the twenty-six (n=26) two-layered tests run at the 0.005 s^{-1} target loading rate, eighteen (n=18) samples failed in the fibrous layer and eight (n=8) samples failed in the chondrogenic layer. Of the thirty (n=30) tests run at the 0.5 s^{-1} target loading rate, twenty-three (n=23) samples failed at the fibrous layer and seven (n=7) samples failed at the chondrogenic layer. It may be possible that the natural curvature of the cartilage coupons before loading may have influenced the primary failure layer. Samples were noted to curl towards the fibrous layer of the perichondrium after fabrication and progressively warp until they were tested. The samples were straightened before testing by applying a small pre-load to eliminate slack and sample curvature. It is possible samples experienced a higher level of tension on the side of the fibrous layer when straightened in the material testing system, causing the fibrous side to start the test with a larger preload than the chondrogenic side, and promoting failure on the side experiencing the greater load first. The tendency of costal cartilage to curve after slicing was studied by Ors [66]. They investigated

warping over time of costal cartilage interstitial matrix grafts made from peripheral and central levels of interstitial matrix. While all samples showed some form of warping, those made from the peripheral interstitial matrix location were observed to begin curling towards the perichondrium layer as soon as 30 minutes after fabrication.

When comparing two-layered and one-layered samples, slight differences in material properties were noticeable, even if not consistently found to have statistical significance. Comparing matched sample type data from this study and Nowinski et al. (costal cartilage interstitial matrix) that all came from the same donors supports the concept that material properties change across depths and layers of the costal cartilage (Figure 32) [25]. The elastic modulus and failure stress were greatest in the perichondrium layers and lowest in the interstitial matrix. Failure strain was the lowest in the fiber layer of the perichondrium and greatest in the interstitial matrix. Despite this, no meaningful difference in SED was seen between layers. This meant that all three layers absorbed approximately the same amount of energy prior to failure. To reach the same amount of energy absorption, the most internal layers experienced higher strain while the external layers experienced higher stress. The costal cartilage, then, had uniform energy absorption potential throughout all of its layers.

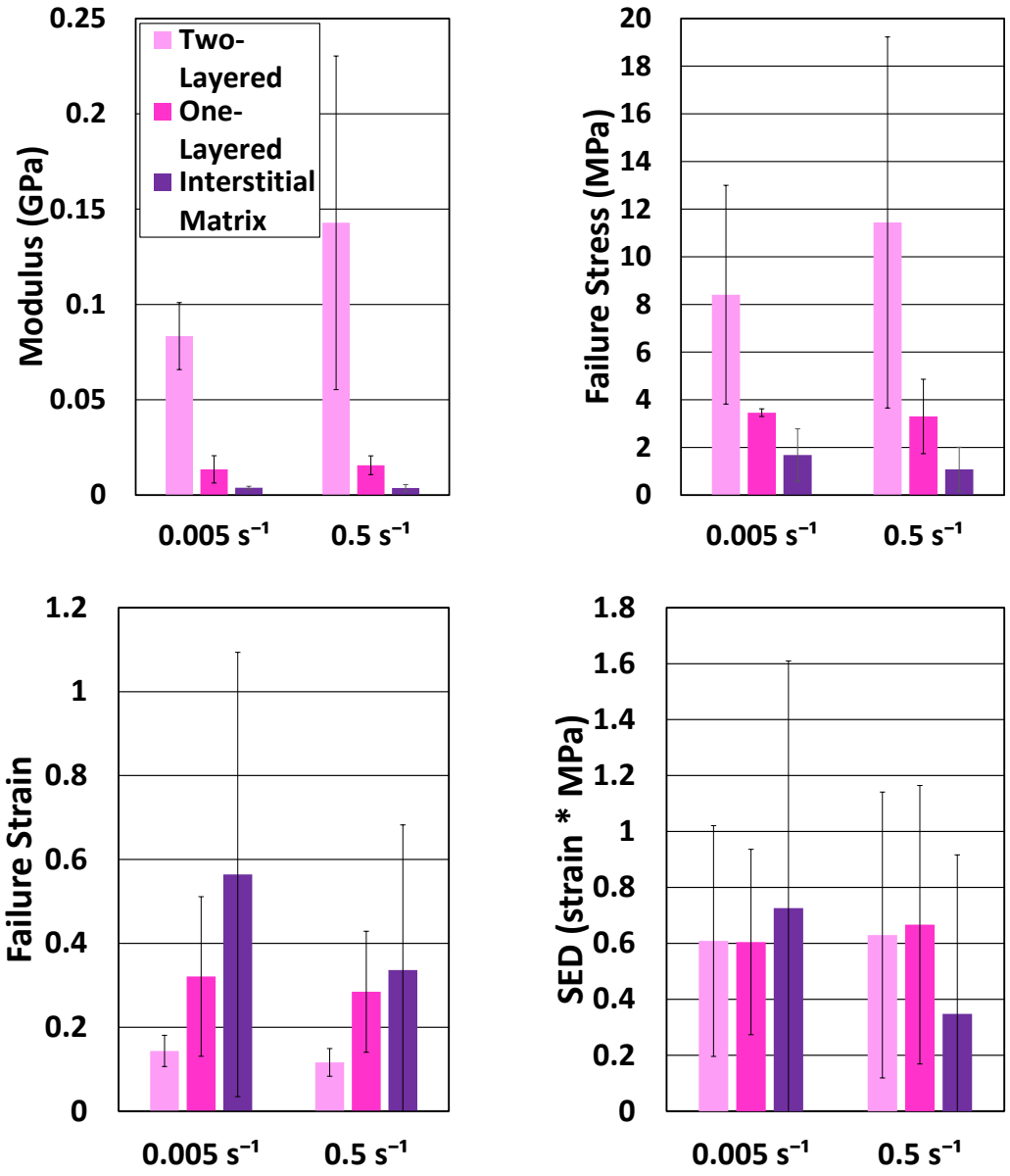

Figure 32. Average and standard deviations of material property data for two- and one-layered perichondrium and interstitial matrix samples that are matched by donor.

This pattern of material property differences with cartilage layers has been observed in studies on articular cartilage. Kempson et al. also studied the role of interstitial matrix depth on fracture stress. Superficial cartilage samples (closer to the perichondrium) had higher fracture stress values than their mid-depth counterparts at the same age. This is consistent with the findings of the current study in that the outer layers of the cartilage have greater failure stresses than samples taken from inner layers and the interstitial matrix. Woo et al. conducted tension testing to failure on 75 samples

of bovine articular cartilage [67]. Samples were taken from the surface, middle, and deep zones of the cartilage and failure stresses and strains were calculated. Interestingly, they found the highest ultimate stress values came from the middle zone, while ultimate stress was lower for the deep and surface zones.

The concept that the fibrous layer of the perichondrium in particular significantly influences structural and material properties has already been investigated. Forman et al. conducted three-point bending tests on human costal cartilage with and without the perichondrium fibrous layer [41]. They found that the fibrous layer contributed nearly 47% of reaction forces in bending. Similarly, Tekke et al. conducted bending tests on human septal cartilage, which is a hyaline cartilage, with and without the perichondrium [45]. It is possible that Tekke et al. only removed the fibrous layer of the perichondrium, as Forman et al. did, but reviewing their methods did not provide clarification on this. Deflection, bending strength, and modulus of elasticity were calculated from these tests. The modulus of elasticity for the costal cartilage with perichondrium was found to be 0.81 MPa and cartilage without the perichondrium had an average modulus value of 0.66 MPa. This study also shows that the perichondrium increases tensile elastic modulus values in cartilage. The perichondrium was found to increase septal cartilage bending strength by 25%.

The role of the perichondrium layer has been investigated in other mammalian cartilages as well. Sun et al. investigated the tensile and compressive elastic modulus of auricular (elastic) cartilage of rabbits with and without the perichondrium [46]. The tensile modulus for samples without perichondrium averaged at 25.37 MPa, and samples with the perichondrium averaged at a modulus of 33.08 MPa. This study further shows the contribution of the perichondrium to the modulus. Since auricular cartilage is an elastic cartilage, there are fundamental differences in the microstructure that make the structural and material properties differ from hyaline cartilages. Differences in magnitudes could also be due to the fact that the tissue came from rabbits rather than humans.

For this study, pre-existing cracks were observed in some two-layered samples from donors over 40 years of age. These samples also tended to fail in the chondrogenic layer first. It is hypothesized that the pre-existing crack phenomenon is associated with cartilage dehydration with age. Patellar cartilage has been shown to dehydrate with age, and it is reasonable to assume that the same phenomenon occurs in costal cartilage [23]. The pre-existing cracks within costal cartilage

perichondrium samples indicate strong age-related changes in the chondrogenic layer. Yet, there were no significant differences in material properties between samples with and without pre-existing cracks. Additionally, all material property trends with donor age aligned between samples with and without pre-existing cracks. It can be inferred from these results that the chondrogenic layer of the perichondrium begins to deteriorate with age, just as the interstitial matrix has been shown to do [25]. This deterioration includes dehydration that leads to the development of internal failures, or pre-existing cracks. The fibrous layer in turn takes on a greater portion of the loading with increasing age. Since changes in material properties with age were still observed for samples with pre-existing cracks, it is likely that changes in both the fibrous and chondrogenic layers are occurring with age. The heavy dependence on the perichondrium fibrous layer for material and structural stability should be investigated further.

Since this study was conducted on human tissue, it was limited to the donors available at the time of testing. Cartilage was not harvested from a consistent rib level and the effect of different levels was not investigated in this study. However, previous work on rib cortical bone material properties has indicated that material properties did not significantly vary with rib level [56]. Therefore, it was assumed that costal cartilage material properties did not vary with rib level for the true ribs (levels 3-7), and testing was limited to these levels. As discussed above, different subgroups of the data (i.e., loading rate and sample type) comprised of different distributions of individuals, which could influence the material property values. The current study featured a bias towards male donors for the fifties and female donors in the sixties. The number of successful tests performed at the 0.005 s^{-1} target loading rate was lower than the number at the 0.5 s^{-1} target loading rate. The presence of calcifications in cartilage from older donors made it difficult to fabricate samples from these subjects. Therefore, there were not any viable samples from donors beyond 69 years of age. It also meant that the characteristic calcifications typically observed in older costal cartilage are not represented in this study. The absence of data from these older donors could influence the observed age trends.

Future work should investigate the different layers of the perichondrium with larger sample sizes to allow for more robust matched data comparisons. The influence of calcifications on tensile material properties of the perichondrium should also be investigated in the future. Ideally, the fibrous layer of the perichondrium should be isolated without damage for further material testing;

however, this may not be possible. The compressive properties of the costal cartilage perichondrium have not yet been studied, but the fibrous nature of the perichondrium implies it would behave differently in compression compared to tension, perhaps more so than the interstitial matrix layer.

Conclusions

This study investigated the tensile material properties of human costal cartilage perichondrium. Samples made from either the chondrogenic layer alone or both the fiber and chondrogenic layers of the perichondrium enabled comparison between cartilage layers. The effect of loading rate was not found to be significant for all but two of the material properties. In general, the material properties decreased with increasing donor age, which agrees with the trends found in existing costal cartilage literature. It is likely that these trends are due to age-related changes in the fibrous and chondrogenic layers. Costal cartilage material properties were found to be different at each layer of the material: interstitial matrix, chondrogenic layer, and fibrous layer. Stresses and modulus were greater in the outer layers, while strains were greater in the inner layers. Overall, the data from this study should be incorporated into human body models to improve their accuracy in costal cartilage failure and injury prediction.

REFERENCES

[1] "WISQARS Leading Causes of Death Visualization Tool," Centers for Disease Control and Prevention. Accessed: Mar. 17, 2024. [Online]. Available: https://wisqars.cdc.gov/lcd/

[2] "WISQARS Leading Causes of Nonfatal Injury," Centers for Disease Control and Prevention. Accessed: Mar. 17, 2024. [Online]. Available: https://wisqars.cdc.gov/lcnf/

[3] A. Mallory, A. Kender, and K. Moorhouse, "Opportunities for crash and injury reduction: A multiharm approach for crash data analysis," *Traffic Inj. Prev.*, vol. 18, no. sup1, pp. S1–S8, May 2017, doi: 10.1080/15389588.2017.1309651.

[4] H. R. Champion, W. S. Copes, W. J. Sacco, M. M. Lawnick, S. L. Keast, and C. F. Frey, "The Major Trauma Outcome Study: Establishing National Norms for Trauma Care," *J. Trauma Acute Care Surg.*, vol. 30, no. 11, p. 1356, Nov. 1990.

[5] M. T. Nummela, F. V. Bensch, T. T. Pyhältö, and S. K. Koskinen, "Incidence and Imaging Findings of Costal Cartilage Fractures in Patients with Blunt Chest Trauma: A Retrospective Review of 1461 Consecutive Whole-Body CT Examinations for Trauma," *Radiology*, vol. 286, no. 2, pp. 696–704, Feb. 2018, doi: 10.1148/radiol.2017162429.

[6] T. Leport, P. Baudrit, P. Potier, X. Trosseille, E. Lecuyer, and G. Vallancien, "Study of Rib Fracture Mechanisms Based on the Rib Strain Profiles in Side and Forward Oblique Impact," SAE International, Warrendale, PA, SAE Technical Paper 2011-22–0009, Nov. 2011. doi: 10.4271/2011-22-0009.

[7] D. Bose, J. Crandall, J. Forman, D. Longhitano, and C. Arregui-Dalmases, "Epidemiology of injuries sustained by rear-seat passengers in frontal motor vehicle crashes," *J. Transp. Health*, vol. 4, pp. 132–139, Mar. 2017, doi: 10.1016/j.jth.2016.10.005.

[8] J. Jermakian, M. Edwards, S. Fein, and M. R. Maltese, "Factors contributing to serious and fatal injuries in belted rear seat occupants in frontal crashes," *Traffic Inj. Prev.*, vol. 20, no. sup1, pp. S84–S91, Jun. 2019, doi: 10.1080/15389588.2019.1601182.

[9] M. Sirmali *et al.*, "A comprehensive analysis of traumatic rib fractures: morbidity, mortality and management," *Eur. J. Cardiothorac. Surg.*, vol. 24, no. 1, pp. 133–138, Jul. 2003, doi: 10.1016/S1010-7940(03)00256-2.

[10] "Abbreviated Injury Scale: 2015 Revision (6 ed.)." Association for the Advancement of Automotive Medicine, 2018.

[11] L. Edgecombe, D. F. Sigmon, M. A. Galuska, and L. D. Angus, “Thoracic Trauma,” in *StatPearls*, Treasure Island (FL): StatPearls Publishing, 2024. Accessed: Mar. 18, 2024. [Online]. Available: http://www.ncbi.nlm.nih.gov/books/NBK534843/

[12] A. I. Caplan, “Cartilage,” *Sci. Am.*, vol. 251, no. 4, pp. 84–97, 1984.

[13] T. Laor and D. Jaramillo, “It’s time to recognize the perichondrium,” *Pediatr. Radiol.*, vol. 50, no. 2, pp. 153–160, Feb. 2020, doi: 10.1007/s00247-019-04534-x.

[14] R. Mallinger and L. Stockinger, “Amianthoid (Asbestoid) transformation: Electron microscopical studies on aging human costal cartilage,” *Am. J. Anat.*, vol. 181, no. 1, pp. 23–32, 1988, doi: 10.1002/aja.1001810104.

[15] A. J. Hough, F. C. Mottram, and L. Sokoloff, “The Collagenous Nature of Amianthoid Degeneration of Human Costal Cartilage,” *Am. J. Pathol.*, vol. 73, no. 1, pp. 201–216, Oct. 1973.

[16] D. W. L. Hukins, D. P. Knight, and J. Woodhead-Galloway, “Amianthoid Change: Orientation of Normal Collagen Fibrils During Aging,” *Science*, vol. 194, no. 4265, pp. 622–624, 1976.

[17] J. H. Stewart and W. F. McCormick, “A sex- and age-limited ossification pattern in human costal cartilages,” *Am. J. Clin. Pathol.*, vol. 81, no. 6, pp. 765–769, Jun. 1984, doi: 10.1093/ajcp/81.6.765.

[18] O. Rejtarová, D. Slízová, P. Smoranc, P. Rejtar, and J. Bukac, “Costal cartilages--a clue for determination of sex,” *Biomed. Pap. Med. Fac. Univ. Palacky Olomouc Czechoslov.*, vol. 148, no. 2, pp. 241–243, Dec. 2004, doi: 10.5507/bp.2004.050.

[19] A. Lau, M. L. Oyen, R. W. Kent, D. Murakami, and T. Torigaki, “Indentation stiffness of aging human costal cartilage,” *Acta Biomater.*, vol. 4, no. 1, pp. 97–103, Jan. 2008, doi: 10.1016/j.actbio.2007.06.008.

[20] F. K. Ontell, E. H. Moore, J. A. Shepard, and D. K. Shelton, “The costal cartilages in health and disease,” *Radiogr. Rev. Publ. Radiol. Soc. N. Am. Inc*, vol. 17, no. 3, pp. 571–577, 1997, doi: 10.1148/radiographics.17.3.9153697.

[21] J. L. Forman and R. W. Kent, “The effect of calcification on the structural mechanics of the costal cartilage,” *Comput. Methods Biomech. Biomed. Engin.*, vol. 17, no. 2, pp. 94–107, Jan. 2014, doi: 10.1080/10255842.2012.671307.

[22] X. Wang *et al.*, “Mechanical properties of extensive calcified costal cartilage: An experimental study,” *Heliyon*, vol. 9, no. 2, p. e13656, 2023, doi: https://doi.org/10.1016/j.heliyon.2023.e13656.

[23] M. F. Venn, “Variation of chemical composition with age in human femoral head cartilage.,” *Ann. Rheum. Dis.*, vol. 37, no. 2, pp. 168–174, Apr. 1978.

[24] B. Guo, D. Liao, X. Li, Y. Zeng, and Q. Yang, “Age and gender related changes in biomechanical properties of healthy human costal cartilage,” *Clin. Biomech. Bristol Avon*, vol. 22, no. 3, pp. 292–297, Mar. 2007, doi: 10.1016/j.clinbiomech.2006.10.004.

[25] H. M. Nowinski, “Effects of Sex, Strain Rate, and Age on the Compressive and Tensile Material Properties of Human Costal Cartilage,” Virginia Tech, 2022. Accessed: Apr. 15, 2024. [Online]. Available: http://hdl.handle.net/10919/115593

[26] M. F. Griffin, G. O’Toole, W. Sabbagh, M. Szarko, and P. E. Butler, “Comparison of the compressive mechanical properties of auricular and costal cartilage from patients with microtia,” *J. Biomech.*, vol. 103, p. 109688, Apr. 2020, doi: 10.1016/j.jbiomech.2020.109688.

[27] S. Tripathy and E. J. Berger, “Quasi-linear viscoelastic properties of costal cartilage using atomic force microscopy,” *Comput. Methods Biomech. Biomed. Engin.*, vol. 15, no. 5, pp. 475–486, 2012, doi: 10.1080/10255842.2010.545820.

[28] J. Feng *et al.*, “The biomechanical, morphologic, and histochemical properties of the costal cartilages in children with pectus excavatum,” *J. Pediatr. Surg.*, vol. 36, no. 12, pp. 1770–1776, Dec. 2001, doi: 10.1053/jpsu.2001.28820.

[29] D. Hanci, O. Üstün, A. B. Yilmazer, A. E. Göker, T. L. Kumral, and Y. Uyar, “Costal Cartilage and Costal Perichondrium Sandwich Graft in Septal Perforation Repair,” *J. Craniofac. Surg.*, vol. 31, no. 5, p. 1327, Aug. 2020, doi: 10.1097/SCS.0000000000006320.

[30] Y. Shi, R. Guo, Q. Hou, H. Hu, H. Wang, and H. Jiang, “The Effect of Perichondrium on Biological and Biomechanical Properties of Molded Diced Cartilage Grafts,” *Aesthetic Plast. Surg.*, vol. 44, no. 2, pp. 549–557, Apr. 2020, doi: 10.1007/s00266-019-01581-5.

[31] D. M. Toriumi, Q. M. Cappelle, and V. Chung, “Use of Costal Perichondrium as an Interpositional Graft for Septal Perforation Closure,” *JAMA Facial Plast. Surg.*, Mar. 2017, doi: 10.1001/jamafacial.2016.1367.

[32] M. J. Duncan, H. G. Thomson, and J. F. Kent Mancer, “Free Cartilage Grafts: The Role of Perichondrium,” *Plast. Reconstr. Surg.*, vol. 73, no. 6, p. 916, Jun. 1984.

[33] M. Kon and A. van den Hooff, “Cartilage Tube Formation by Perichondrium: A New Concept for Tracheal Reconstruction,” *Plast. Reconstr. Surg.*, vol. 72, no. 6, p. 791, Dec. 1983.

[34] S. R. Akkina and S. P. Most, “The effect of perichondrium on cartilage graft properties,” *Curr. Opin. Otolaryngol. Head Neck Surg.*, vol. 30, no. 4, p. 215, Aug. 2022, doi: 10.1097/MOO.0000000000000812.

[35] S. K. Bulstra, G. N. Homminga, W. A. Buurman, E. Terwindt-Rouwenhorst, and A. J. van der Linden, “The potential of adult human perichondrium to form hyalin cartilage in vitro,” *J. Orthop. Res.*, vol. 8, no. 3, pp. 328–335, 1990, doi: 10.1002/jor.1100080304.

[36] “Regenerative Potential of Perichondrium: A Tissue Engineering Perspective | Tissue Engineering Part B: Reviews.” Accessed: Apr. 24, 2024. [Online]. Available: https://www.liebertpub.com/doi/full/10.1089/ten.teb.2021.0054

[37] L. Ohlsén, “CARTILAGE REGENERATION FROM PERICHONDRIUM,” *Plast. Reconstr. Surg.*, vol. 62, no. 4, p. 507, Oct. 1978.

[38] J. Yang, L. Lin, Y. Zhang, Y. Wang, L. Cui, and L. He, “The Regenerated Tissue at the Donor Site After Costal Cartilage Harvest for Auricular Reconstruction,” *J. Craniofac. Surg.*, vol. 30, no. 6, p. e490, Sep. 2019, doi: 10.1097/SCS.0000000000005370.

[39] Z. Piao *et al.*, “The Response of Costal Cartilage to Mechanical Injury in Mice,” *Plast. Reconstr. Surg.*, vol. 119, no. 3, p. 830, Mar. 2007, doi: 10.1097/01.prs.0000240817.11002.3e.

[40] M. L. G. Duynstee, H. L. Verwoerd-Verhoef, C. D. A. Verwoerd, and G. J. V. M. van Osch, “The Dual Role of Perichondrium in Cartilage Wound Healing,” *Plast. Reconstr. Surg.*, vol. 110, no. 4, p. 1073, Sep. 2002, doi: 10.1097/01.PRS.0000020991.10201.6C.

[41] J. L. Forman, E. del Pozo de Dios, C. A. Dalmases, and R. W. Kent, “The contribution of the perichondrium to the structural mechanical behavior of the costal-cartilage,” *J. Biomech. Eng.*, vol. 132, no. 9, p. 094501, Sep. 2010, doi: 10.1115/1.4001976.

[42] A. Gradischar *et al.*, “Measurement of global mechanical properties of human thorax: Costal cartilage,” *J. Biomech.*, vol. 142, p. 111242, Sep. 2022, doi: 10.1016/j.jbiomech.2022.111242.

[43] R. Roy *et al.*, “Analysis of bending behavior of native and engineered auricular and costal cartilage,” *J. Biomed. Mater. Res. A*, vol. 68, no. 4, pp. 597–602, Mar. 2004, doi: 10.1002/jbm.a.10068.

[44] S. S. Kohles, “Application of flexural and membrane stress analysis to distinguish tensile and compressive moduli of biologic materials,” *J. Mech. Behav. Biomed. Mater.*, vol. 119, p. 104474, Jul. 2021, doi: 10.1016/j.jmbbm.2021.104474.

[45] N. S. Tekke *et al.*, “Importance of nasal septal cartilage perichondrium for septum strength mechanics: a cadaveric study,” *Rhinology*, vol. 52, no. 2, pp. 167–171, Jun. 2014, doi: 10.4193/Rhino13.199.

[46] H. Sun, J. Zhou, Q. Wang, H. Jiang, and Q. Yang, “Contribution of perichondrium to the mechanical properties of auricular cartilage,” *J. Biomech.*, vol. 126, p. 110638, Sep. 2021, doi: 10.1016/j.jbiomech.2021.110638.

[47] “GHBMC.” Accessed: Apr. 27, 2024. [Online]. Available: https://www.ghbmc.com/

[48] “The SAFER Human Body Model is going global to save more lives in traffic | Safer.” Accessed: Apr. 27, 2024. [Online]. Available: https://www.saferresearch.com/news/safer-human-body-model-going-global-save-more-lives-traffic

[49] J. John, C. Klug, M. Kranjec, E. Svenning, and J. Iraeus, “Hello, world! VIVA+: A human body model lineup to evaluate sex-differences in crash protection,” *Front. Bioeng. Biotechnol.*, vol. 10, Jul. 2022, doi: 10.3389/fbioe.2022.918904.

[50] “THUMS | Toyota Motor Corporation.” Accessed: Apr. 27, 2024. [Online]. Available: https://www.toyota.co.jp/thums/

[51] Y. Takahira *et al.*, “Investigation of Effective Restraining Force on Rib Fracture Risk Reduction for Elderly Occupant in Frontal Collision,” 2022, [Online]. Available: https://www.ircobi.org/wordpress/downloads/irc22/pdf-files/2296.pdf

[52] Y. Takahira, S. Akima, Y. Kusuhara, N. Tanase, and Y. Kitagawa, “Cross-Sectional Analysis of Rib Fracture Mechanism of Elderly Occupant in Frontal Collision using THUMS,” 2021.

[53] E. Mishra, K. Mroz, B. Pipkorn, and N. Lubbe, “Effects of Automated Emergency Braking and Seatbelt Pre-Pretensioning on Occupant Injury Risks in High-Severity Frontal Crashes,” *Front. Future Transp.*, vol. 3, Jun. 2022, doi: 10.3389/ffutr.2022.883951.

[54] M. Östling, C. Lundgren, N. Lubbe, and B. Pipkorn, “Reducing Lumbar Spine Vertebra Fracture Risk With an Adaptive Seat Track Load Limiter,” *Front. Future Transp.*, vol. 3, Jun. 2022, doi: 10.3389/ffutr.2022.890117.

[55] K. Mroz *et al.*, “Effect of Seat and Seat Belt characteristics on the Lumbar Spine and Pelvis Loading of the SAFER Human Body Model in reclined Postures,” 2020.

[56] A. R. Kemper *et al.*, “Material properties of human rib cortical bone from dynamic tension coupon testing,” *Stapp Car Crash J.*, vol. 49, pp. 199–230, Nov. 2005, doi: 10.4271/2005-22-0010.

[57] A. R. Kemper, C. McNally, C. A. Pullins, L. J. Freeman, S. M. Duma, and S. W. Rouhana, “The Biomechanics of Human Ribs: Material and Structural Properties from Dynamic Tension and Bending Tests,” SAE International, Warrendale, PA, SAE Technical Paper 2007-22–0011, Oct. 2007. doi: 10.4271/2007-22-0011.

[58] D. Albert, Y.-S. Kang, A. Agnew, and A. Kemper, “A Comparison of Rib Structural and Material Properties from Matched Whole Rib Bending and Tension Coupon Tests,” 2017.

[59] M. J. Katzenberger, D. L. Albert, A. M. Agnew, and A. R. Kemper, “Effects of sex, age, and two loading rates on the tensile material properties of human rib cortical bone,” *J. Mech. Behav. Biomed. Mater.*, vol. 102, p. 103410, Feb. 2020, doi: 10.1016/j.jmbbm.2019.103410.

[60] M. A. Corrales, J. H. Bolte, B. Pipkorn, C. Markusic, and D. S. Cronin, “Explaining and predicting the increased thorax injury in aged females: age and subject-specific thorax geometry coupled with improved bone constitutive models and age-specific material properties evaluated in side impact conditions,” *Front. Public Health*, vol. 12, Mar. 2024, doi: 10.3389/fpubh.2024.1336518.

[61] D. S. Cronin, B. Watson, F. Khor, D. Gierczycka, and S. Malcolm, “Cortical bone continuum damage mechanics constitutive model with stress triaxiality criterion to predict fracture initiation and pattern,” *Front. Bioeng. Biotechnol.*, vol. 10, Oct. 2022, doi: 10.3389/fbioe.2022.1022506.

[62] K.-J. Larsson, J. Iraeus, S. Holcombe, and B. Pipkorn, “Influences of human thorax variability on population rib fracture risk prediction using human body models,” *Front. Bioeng. Biotechnol.*, vol. 11, Mar. 2023, doi: 10.3389/fbioe.2023.1154272.

[63] “SAE MOBILUS.” Accessed: Apr. 26, 2024. [Online]. Available: https://saemobilus-sae-org.ezproxy.lib.vt.edu/content/J211/1_202208/

[64] D. M. Elliott, D. A. Narmoneva, and L. A. Setton, “Direct Measurement of the Poisson’s Ratio of Human Patella Cartilage in Tension,” *J. Biomech. Eng.*, vol. 124, no. 2, pp. 223–228, Mar. 2002, doi: 10.1115/1.1449905.

[65] G. E. Kempson, “Age-related changes in the tensile properties of human articular cartilage: a comparative study between the femoral head of the hip joint and the talus of the ankle joint,” *Biochim. Biophys. Acta*, vol. 1075, no. 3, pp. 223–230, Oct. 1991, doi: 10.1016/0304-4165(91)90270-q.

[66] S. Ors, “Measurement of Warping Angle in Human Rib Graft: An Experimental Study,” *Plast. Reconstr. Surg.*, vol. 141, no. 5, pp. 1147–1157, May 2018, doi: 10.1097/PRS.0000000000004316.

[67] S. L.-Y. Woo, W. H. Akeson, and G. F. Jemmott, “Measurements of nonhomogeneous, directional mechanical properties of articular cartilage in tension,” *J. Biomech.*, vol. 9, no. 12, pp. 785–791, Jan. 1976, doi: 10.1016/0021-9290(76)90186-X.

APPENDIX

Table A1. Subject characteristics and successful two- and one-layered tests.

Subject Number	Age (years)	Sex	Weight (kg)	Height (cm)	Successful 0.005 s^{-1} Two-Layered Test	Successful 0.5 s^{-1} Two-Layered Test	Successful 0.005 s^{-1} One-Layered Test	Successful 0.5 s^{-1} One-Layered Test
CC-2	11	F	50.50	160.20	XX	X	X	X
CC-5	14	M	167.64	60.01		X		
CC-10	17	F	76.00	165.00	X	X		
CC-9	17	M	77.11	177.80	X	X		
CC-15	19	M	77.60	177.80	X	X		
CC-17	20	F	48.90	165.10	X	XX		
CC-33	24	M	75.30	163.83		X	X	X
CC-27	27	M	182.00	73.00	X	X	X	
CC-52	28	F	90.70	157.48		X		
CC-29	30	M	172.72	83.46		X		
CC-31	31	F	154.94	67.99				X
CC-53	33	F	157.48	63.50		XX		
CC-54	35	F	68.04	167.64	X	X		
CC-36	35	M	171.45	96.16	XXX	X	X	X
CC-55	38	F	91.63	175.30	X			
CC-56	39	M	174.00	59.90	X	X		
CC-40	43	F	55.20	162.60		X		
CC-42	45	M	113.40	182.90	X			
CC-43	46	M	75.88	168.00	X	X		
CC-47	48	F	43.00	157.50		X		
CC-49	48	M	183.64	63.04	XX	XX		X
CC-50	49	F	93.21	177.80	X			
CC-57	49	M	182.88	90.71		X		
CC-58	51	M	105.20	193.00		X		
CC-59	53	M	172.70	82.10		X		
CC-60	54	F	76.20	162.56	XX	X		X
CC-61	54	M	93.89	177.80	X	X		X
CC-62	57	M	61.23	187.96	X			
CC-63	59	M	185.42	72.57	X			
CC-64	60	F	46.49	161.29	X	X		
CC-65	67	F	165.10	64.41	X	X		
CC-66	69	F	43.54	161.29	X	X		
CC-67	69	M	182.88	88.90		X		

Note: X = one (1) successful test, XX = two (2) successful tests averaged, XXX = three (3) successful tests averaged

Table A2. Results from the Shapiro-Wilk Test of Normality for two-layered samples.

Material Property Variable	0.005 s^{-1}		0.5 s^{-1}	
	W	p-value	W	p-value
Age	0.9508	0.3519	0.9555	0.2909
Modulus	0.7961	**0.0006**	0.9460	0.1708
Ultimate Stress	0.8206	**0.0014**	0.8807	**0.0050**
Ultimate Strain	0.9587	0.4904	0.9597	0.3634
Failure Stress	0.8136	**0.0011**	0.8795	**0.0047**
Failure Strain	0.9465	0.2918	0.9712	0.6343
SED	0.8840	0.0174	0.8115	**0.0002**

Table A3. Results from the Shapiro-Wilk Test of normality for one-layered samples.

Material Property Variable	0.005 s^{-1}		0.5 s^{-1}	
	W	p-value	W	p-value
Age	0.9666	0.8204	0.9256	0.5141
Modulus	0.9410	0.6602	0.8677	0.1771
Ultimate Stress	0.7995	0.1014	0.8879	0.2639
Ultimate Strain	0.7592	**0.0469**	0.9162	0.4407
Failure Stress	0.6753	**0.0058**	0.9037	0.3538
Failure Strain	0.7072	**0.0141**	0.9145	0.4280
SED	0.8040	0.1240	0.9408	0.6462

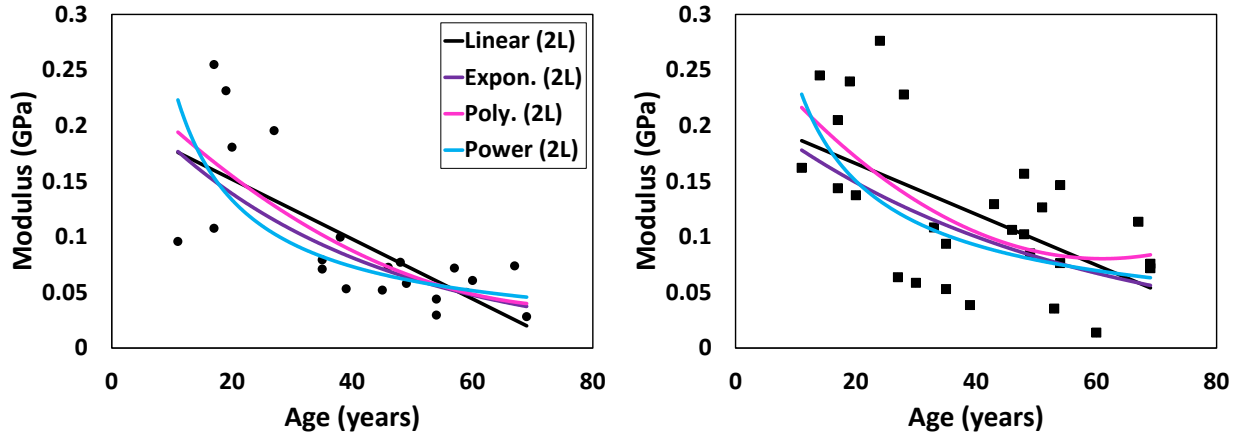

Figure 33. Elastic modulus vs. age of two-layered perichondrium samples, with the 0.005 s^{-1} target loading rate on the left and 0.5 s^{-1} on the right. Different trend line types are represented by different colors (black = linear, purple = exponential, pink = quadratic, blue = power).

Table A4. Equations and R^2 values using different types of trend lines for the elastic modulus vs. age of two-layered samples. The largest R^2 value is shown in bold text.

		Linear	**Exponential**	**Quadratic**	**Power**
0.005 s^{-1}	Equation	$y = -0.0027x + 0.2054$	$y = 0.2373e^{-0.027x}$	$y = 4E\text{-}05x^2 - 0.0055x + 0.25$	$y = 1.767x^{-0.863}$
	R^2	0.5297	**0.6028**	0.5521	0.5605
0.5 s^{-1}	Equation	$y = -0.0023x + 0.2116$	$y = 0.2214e^{-0.02x}$	$y = 5E\text{-}05x^2 - 0.0066x + 0.2826$	$y = 1.2212x^{-0.699}$
	R^2	0.3349	0.2643	**0.3857**	0.2888

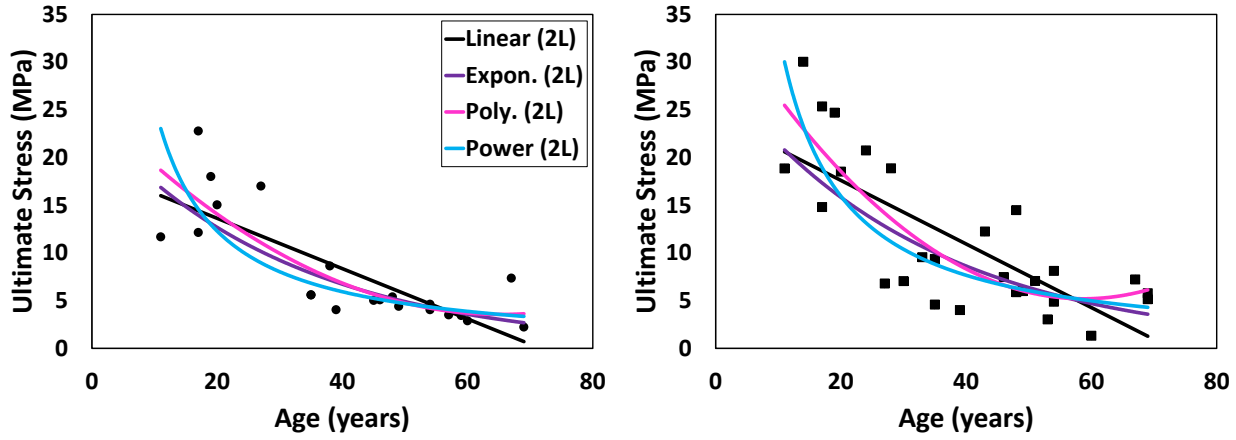

Figure 34. Ultimate stress vs. age of two-layered perichondrium samples, with the 0.005 s^{-1} target loading rate on the left and 0.5 s^{-1} on the right. Different trend line types are represented by different colors (black = linear, purple = exponential, pink = quadratic, blue = power).

Table A5. Equations and R^2 values using different types of trend lines for the ultimate stress vs. age of two-layered samples. The largest R^2 value is shown in bold text.

		Linear	**Exponential**	**Quadratic**	**Power**
0.005 s^{-1}	Equation	$y = -0.2637x + 18.902$	$y = 23.903e^{-0.032x}$	$y = 0.0051x^2 - 0.669x + 25.408$	$y = 285.95x^{-1.05}$
	R^2	0.6363	**0.7208**	0.696	0.7095
0.5 s^{-1}	Equation	$-0.3333x + 24.268$	$29.044e^{-0.03x}$	$y = 0.0089x^2 - 1.0449x + 35.891$	$y = 379.89x^{-1.058}$
	R^2	0.5695	0.5243	**0.678**	0.5605

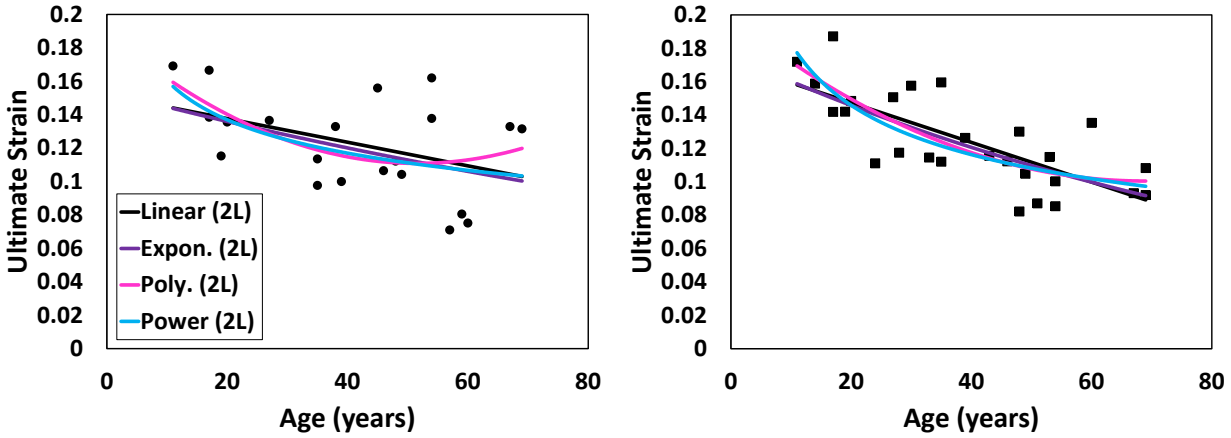

Figure 35. Ultimate strain vs. age of two-layered perichondrium samples, with the 0.005 s^{-1} target loading rate on the left and 0.5 s^{-1} on the right. Different trend line types are represented by different colors (black = linear, purple = exponential, pink = quadratic, blue = power).

Table A6. Equations and R^2 values using different types of trend lines for the ultimate strain vs. age of two-layered samples. The largest R^2 value is shown in bold text.

		Linear	**Exponential**	**Quadratic**	**Power**
0.005 s^{-1}	Equation	$y = -0.0007x + 0.1518$	$y = 0.1539e^{-0.006x}$	$y = 3E\text{-}05x^2 - 0.003x + 0.1892$	$y = 0.2706x^{-0.227}$
	R^2	0.1854	0.1882	**0.2657**	0.2266
0.5 s^{-1}	Equation	$y = -0.0012x + 0.1711$	$y = 0.1761e^{-0.009x}$	$y = 2E\text{-}05x^2 - 0.0028x + 0.1982$	$y = 0.3882x^{-0.327}$
	R^2	0.5455	0.5403	**0.59**	0.5665

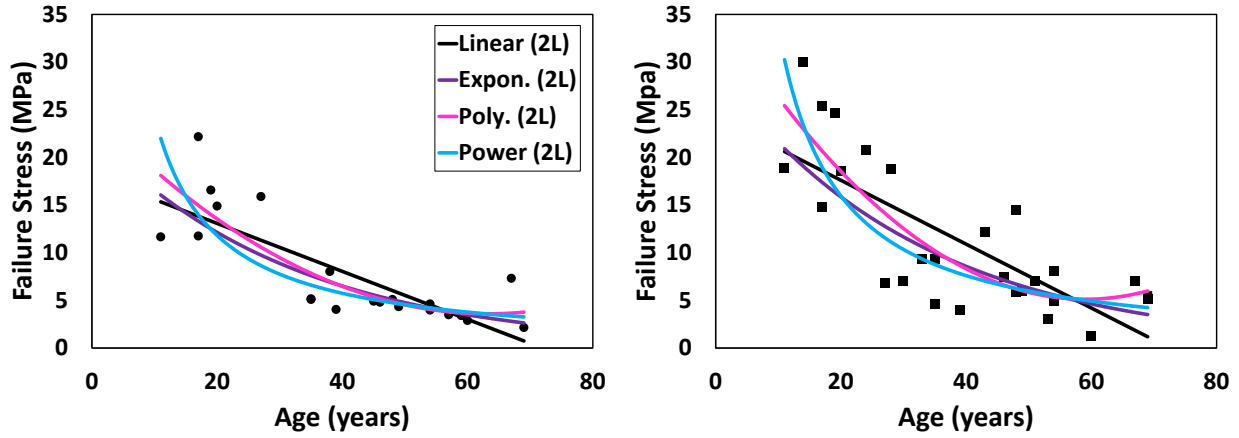

Figure 36. Failure stress vs. age of two-layered perichondrium samples, with the 0.005 s^{-1} target loading rate on the left and 0.5 s^{-1} on the right. Different trend line types are represented by different colors (black = linear, purple = exponential, pink = quadratic, blue = power).

Table A7. Equations and R^2 values using different types of trend lines for the failure stress vs. age of two-layered samples. The largest R^2 value is shown in bold text.

		Linear	**Exponential**	**Quadratic**	**Power**
0.005 s^{-1}	Equation	$y = -0.2517x + 18.105$	$y = 22.618e^{-0.031x}$	$y = 0.0053x^2 - 0.6713x + 24.843$	$y = 266.18x^{-1.04}$
	R^2	0.635	**0.7143**	0.7051	0.7124
0.5 s^{-1}	Equation	$y = -0.335x + 24.296$	$y = 29.336e^{-0.031x}$	$y = 0.0088x^2 - 1.0386x + 35.788$	$y = 393.58x^{-1.07}$
	R^2	0.5738	0.53	**0.6796**	0.5635

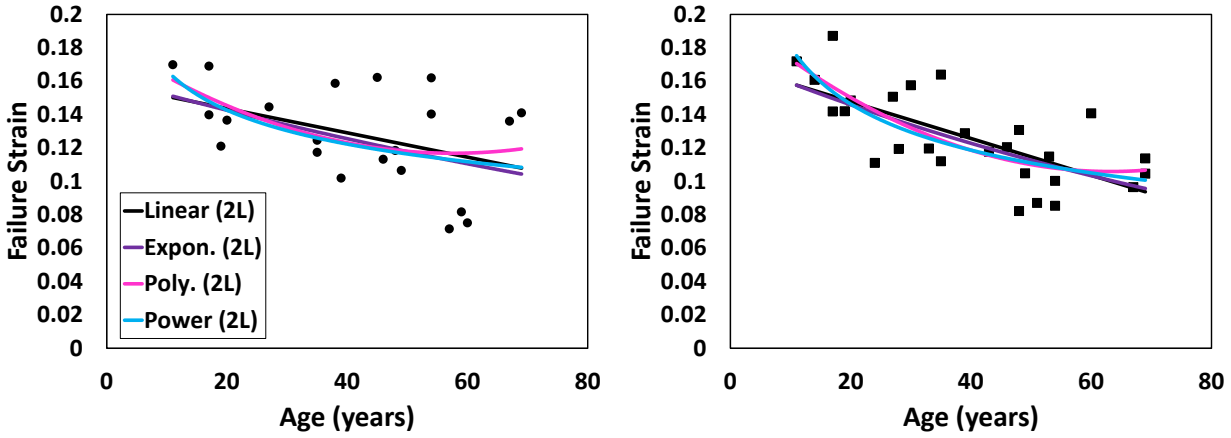

Figure 37. Failure strain vs. age of two-layered perichondrium samples, with the 0.005 s^{-1} target loading rate on the left and 0.5 s^{-1} on the right. Different trend line types are represented by different colors (black = linear, purple = exponential, pink = quadratic, blue = power).

Table A8. Equations and R^2 values using different types of trend lines for the failure strain vs. age of two-layered samples. The largest R^2 value is shown in bold text.

		Linear	**Exponential**	**Quadratic**	**Power**
0.005 s^{-1}	Equation	$y = -0.0007x + 0.1582$	$y = 0.1619e^{-0.006x}$	$y = 2E\text{-}05x^2 - 0.0023x + 0.1839$	$y = 0.2773x^{-0.222}$
	R^2	0.1886	0.1931	**0.2246**	0.2101
0.5 s^{-1}	Equation	$y = -0.0011x + 0.1697$	$y = 0.1733e^{-0.009x}$	$y = 2E\text{-}05x^2 - 0.003x + 0.2007$	$y = 0.3614x^{-0.302}$
	R^2	0.4861	0.4706	**0.5464**	0.5087

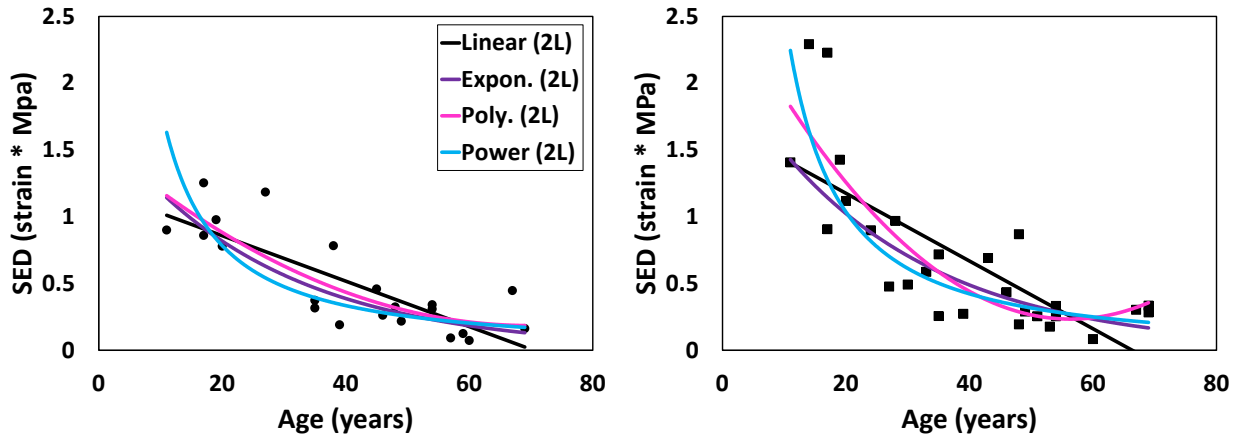

Figure 38. SED vs. age of two-layered perichondrium samples, with the 0.005 s^{-1} target loading rate on the left and 0.5 s^{-1} on the right. Different trend line types are represented by different colors (black = linear, purple = exponential, pink = quadratic, blue = power).

Table A9. Equations and R^2 values using different types of trend lines for the SED vs. age of two-layered samples. The largest R^2 value is shown in bold text.

		Linear	**Exponential**	**Quadratic**	**Power**
0.005 s^{-1}	Equation	$y = -0.017x + 1.198$	$y = 1.7233e^{-0.037x}$	$y = 0.0003x^2 - 0.0393x + 1.5556$	$y = 30.976x^{-1.228}$
	R^2	0.6609	0.6203	**0.7058**	0.6016
0.5 s^{-1}	Equation	$y = -0.0253x + 1.6817$	$y = 2.1442e^{-0.037x}$	$y = 0.0008x^2 - 0.0872x + 2.6921$	$y = 49.968x^{-1.294}$
	R^2	0.5772	0.6294	**0.7148**	0.6776